Cell Reports

Article

Endosymbiont control through non-canonical immune signaling and gut metabolic remodeling

Graphical abstract

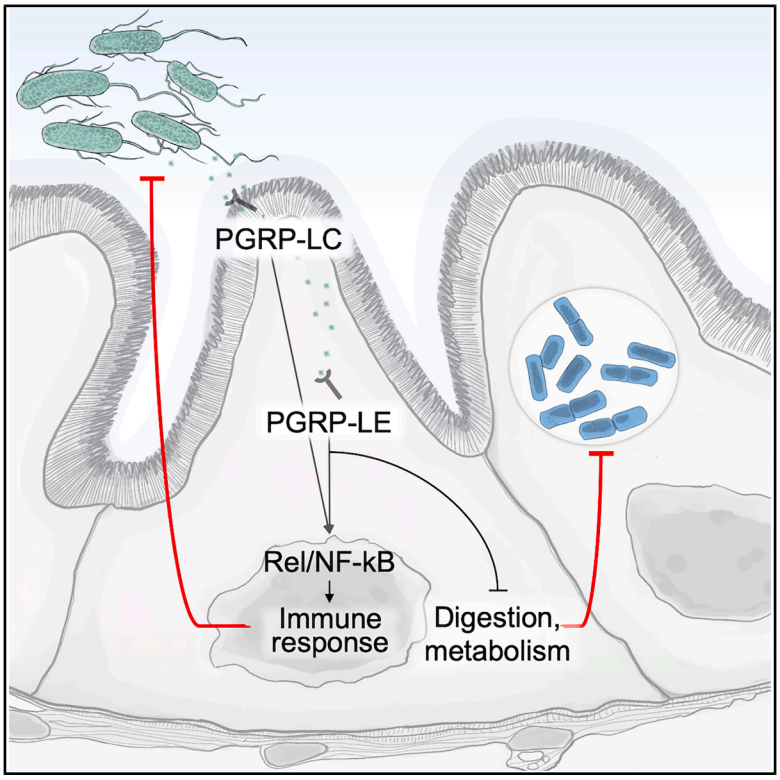

Authors

Sofie Burgmer,
Fenja L. Meyer zu Altenschildesche,
Akos Gyenis, ..., Arnaud Fichant,
Mirka Uhlirova, Gilles Storelli

Correspondence

gilles.storelli@cos.uni-heidelberg.de

In brief

Burgmer et al. show that the pattern recognition receptors (PRRs) PGRP-LC and PGRP-LE repress key metabolic functions in the *Drosophila* midgut. These regulations occur independently of canonical immune pathways and restrict parasitic *Wolbachia* endosymbionts in the intestine and peripheral tissues. Thus, PRRs act beyond canonical immune pathways to control bacteria.

Highlights

- *Drosophila* PGRP-LC and PGRP-LE bind bacterial peptidoglycan
- These receptors act through Rel/NF-κB to induce an immune response in the gut
- PGRP-LC and PGRP-LE suppress intestinal metabolism independently of Rel/NF-κB
- Metabolic remodeling curbs parasitic endosymbionts in the gut and peripheral organs

Burgmer et al., 2025, Cell Reports *44*, 115811
June 24, 2025
https://doi.org/10.1016/j.celrep.2025.115811

CellPress

Cell Reports

CellPress
OPEN ACCESS

Article

Endosymbiont control through non-canonical immune signaling and gut metabolic remodeling

Sofie Burgmer,[1,2] Fenja L. Meyer zu Altenschildesche,[1,2] Akos Gyenis,[3] Hyun Ju Lee,[1,4] David Vilchez,[1,2,4] Patrick Giavalisco,[5] Arnaud Fichant,[6] Mirka Uhlirova,[1,2] and Gilles Storelli[1,2,6,7,*]

[1]Cluster of Excellence Cellular Stress Responses in Aging-associated Diseases (CECAD), Faculty of Mathematics and Natural Sciences, University of Cologne, 50931 Cologne, Germany

[2]Institute for Genetics, Faculty of Mathematics and Natural Sciences, University of Cologne, 50931 Cologne, Germany

[3]Cluster of Excellence Cellular Stress Responses in Aging-associated Diseases (CECAD), Faculty of Medicine and University Hospital of Cologne, University of Cologne, 50931 Cologne, Germany

[4]Institute for Integrated Stress Response Signaling, Faculty of Medicine, University Hospital Cologne, 50931 Cologne, Germany

[5]Max Planck Institute for Biology of Ageing, 50931 Cologne, Germany

[6]Centre for Organismal Studies (COS) Heidelberg, Heidelberg University, 69120 Heidelberg, Germany

[7]Lead contact

*Correspondence: gilles.storelli@cos.uni-heidelberg.de

https://doi.org/10.1016/j.celrep.2025.115811

SUMMARY

Animals coexist with bacteria and need to keep these microorganisms under tight control. To achieve such control, pattern recognition receptors (PRRs) sense bacterial cues and induce the production of antimicrobials. Here, we uncover a metabolic arm in the control of symbionts by PRRs. We show that, in *Drosophila*, the PRRs PGRP-LC and PGRP-LE act independently of canonical NF-κB signaling to repress essential metabolic functions in the gut, such as digestion and central carbon metabolism. This metabolic switch affects commensal populations and drastically reduces intestinal and systemic populations of the intracellular parasite *Wolbachia*. We propose that intestinal metabolic remodeling complements immune responses by imposing nutrient restriction on intracellular bacteria, whose lifestyle protects them from antimicrobials. Our findings reveal a role for PRRs in bacterial control beyond canonical immune pathways and provide insights into how microbial signals modulate symbiotic populations but also nutrition and metabolism in animals.

INTRODUCTION

Animals coexist with bacteria, engaging in symbiotic relationships that range from parasitism to mutualism.[1] In all cases, these interactions rely on strict regulatory mechanisms to prevent infection, with innate immunity playing a central role in multicellular organisms.[2] The innate immune system relies on pattern recognition receptors (PRRs) that recognize conserved microbial motifs, called microbe-associated molecular patterns (MAMPs). MAMP recognition initiates immune responses through the nuclear factor kappa-light-chain-enhancer of activated B cells (NF-κB) signaling pathway. This results in the production of immune effectors, such as antimicrobial peptides (AMPs), to contain early stages of infection or maintain symbiotic homeostasis. These processes are critical in the gut, which houses a wide diversity of commensal microbes while being a major entry point for pathogens. Therefore, dysregulated innate immunity is associated with microbiota dysbiosis but also with intestinal inflammation, malabsorption, and a range of systemic defects.[3–5] Although these observations suggest that innate immune signaling controls major intestinal functions, the complexity of gut ecosystems has made it challenging to establish clear causal relationships between these processes.

Fundamental mechanisms regulating innate immunity were discovered in the invertebrate *Drosophila* before their existence was confirmed in mammals.[6] Toll and Imd are the two pathways controlling innate immunity in these invertebrates. Imd is primarily active in the midgut and is triggered by the recognition of diaminopimelic acid-containing peptidoglycan by the peptidoglycan recognition proteins LC and LE (PGRP-LC/LE). PGRP-LC is a transmembrane receptor, whereas PGRP-LE is cytosolic. Both PRRs are expressed in the midgut, but PGRP-LE primarily regulates Imd signaling in enterocytes (ECs).[7–10] In addition to their PGRP domain, these PRRs contain a cryptic RIP homotypic interaction motif (cRHIM) similar to the RHIM found in several NF-κB signaling components in mammals.[11–13] The cRHIM is required for PGRP-LC and -LE to form an amyloid nucleus.[11,12,14] This structure supports the formation of amyloid fibrils by the adaptor protein Imd, which act as a platform for the recruitment of other signaling components.[11,12,14] This large protein complex ultimately activates the NF-κB transcription factor Relish (Rel/NF-κB), which triggers the production of AMPs.[11,12,14] Beyond their role in innate immunity, recent evidence suggests that *Drosophila* PRRs regulate essential gut functions, including digestion, in response to bacterial cues.[15,16] The extent of

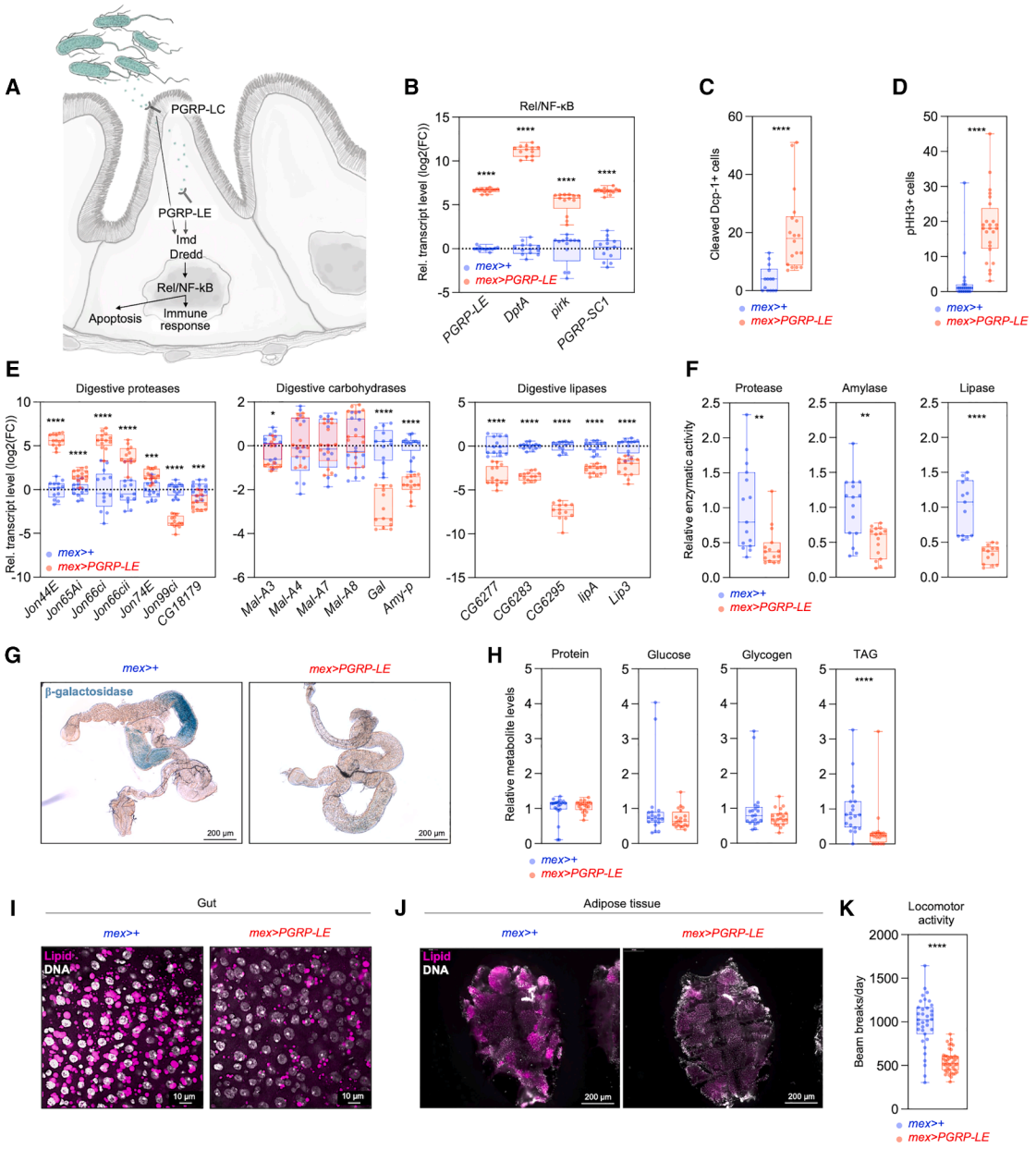

Figure 1. PGRP-LE signaling suppresses digestion

(A) Simplified representation of signaling downstream of PGRP-LC and PGRP-LE in ECs. See main text for details.

(B–K) *PGRP-LE* was overexpressed in ECs by driving the expression of a *UAS-PGRP-LE* transgene with the EC-specific *mex-GAL4* driver (*mex>PGRP-LE*). Controls are animals carrying the *mex-GAL4* driver alone (*mex>+*).

(B) The levels of transcripts regulated by Rel/NF-κB were scored by RT-qPCR in midguts. $n = 13$ biological replicates per genotype.

(C and D) The numbers of (C) apoptotic cells and (D) stem cells undergoing mitosis were scored in the midgut using anti-cleaved Dcp-1 and anti-pHH3 antibody stains, respectively. $24 > n > 14$ midguts.

(E) The levels of representative transcripts encoding digestive proteases, carbohydrases, and lipases were scored in midguts by RT-qPCR. $n = 13$ biological replicates per genotype.

(B and E) Graphs represent log2 fold change (log2(FC)) in transcript levels relative to controls.

(F) Proteolytic, amylolytic, and lipolytic activities were measured in midguts. Enzymatic activities were normalized to the number of tissues and are shown relative to control levels. $15 > n > 13$ biological replicates per genotype.

(G) X-gal stains were used to visualize brush border β-galactosidase activity in midguts. See also Figures S1C and S1D. Scale bar: 200 μm.

(H) Protein, glucose, glycogen, and triacylglycerol (TAG) levels were scored in whole animals. Metabolite levels are normalized to protein content and shown relative to controls. $20 > n > 15$ biological replicates.

(legend continued on next page)

these regulations as well as their contribution to host defense and the maintenance of symbiotic populations remains unclear.

Here, we investigate the non-immune functions of PGRP-LC/LE signaling in the midgut. By genetically manipulating these pathways, we show that PGRP-LC/LE signaling profoundly affects gut function, suppressing key digestive activities and metabolic processes. While this effect may still require the formation of PRR amyloids, it occurs independently of canonical Rel/NF-κB signaling. Thus, PRRs coordinate immune and metabolic responses through distinct pathways. Intestinal metabolic remodeling affects bacterial populations in the gut lumen and drastically reduces the titer of intracellular *Wolbachia* endosymbionts in the midgut but also in distant tissues. We propose that intestinal metabolic remodeling controls endosymbiont growth by limiting nutrient availability. This metabolic response may complement the effect of conventional antimicrobials, from which intracellular bacteria are protected. In summary, our findings reveal a role for PRRs in bacterial control beyond canonical immune pathways and provide insights into how microbial signals modulate host nutrition and metabolism, ultimately impacting symbiotic bacterial populations.

RESULTS

PGRP-LE signaling suppresses digestion

To characterize the role of PRRs in regulating gut function, we sought ways to robustly activate signaling downstream of these receptors. Gavage with gram-negative bacteria is commonly used to activate PRR signaling in the midgut, but variability in microbial ingestion and persistence can lead to inconsistent effects.[17] To overcome these limitations, we overexpressed *PGPR-LE* in ECs of conventionally reared male *Drosophila*. This induces the expression of the Rel/NF-κB targets *DptA*, *pirk*, and *PGRP-SC1* in the midgut, confirming that this genetic manipulation induces immune signaling in the absence of an infection[11,18] (Figures 1A and 1B). It also induces EC apoptosis, consistent with the known effects of Rel activation,[19] and acts in a non-autonomous manner to promote intestinal stem cell mitosis (Figures 1C and 1D). PGRP-LE has been reported previously to activate the expression of several digestive proteases when germ-free animals are re-associated with natural commensals.[15] We therefore scored the effect of *PGRP-LE* overexpression on representative proteases. Consistent with previous studies, we detected significant increases in *Jon44E*, *Jon65Ai*, *Jon66ci*, *Jon66cii*, and *Jon74E* transcripts following *PGRP-LE* overexpression (Figure 1E).[15] However, not all proteases were induced, the transcript levels of *Jon99ci* and *CG18179* being reduced (Figure 1E). We next sought to determine whether PGRP-LE also influences digestive carbohydrases and lipases by scoring the levels of representative transcripts encoding these enzymes. *PGRP-LE* overexpression has mixed impacts on carbohydrases: some transcripts are unaffected (*Mal-A4*, *Mal-A7*, and *Mal-A8*), while others are reduced (*Mal-A3*, *Gal*, and *Amy-p*) (Figure 1E). In contrast, all transcripts encoding digestive lipases that we scored were reduced (Figure 1E). Expressing *PGRP-LE* for 48 h recapitulates most of these effects, indicating that this PRR can rapidly alter the expression of digestive enzymes (Figure S1A). In parallel, *PGRP-LE* overexpression induces similar alterations in females, indicating that these effects are not sex specific (Figure S1B). Since we observed mixed effects on a limited set of transcripts encoding digestive enzymes, we set out to determine the overall impact of PGRP-LE signaling on digestive activities. Using biochemical assays, we detected a significant reduction in total proteolytic, amylolytic, and lipolytic activities in the midgut following *PGRP-LE* overexpression in ECs (Figure 1F). Consistent with the repression of *Gal*, brush border β-galactosidase is also suppressed (Figures 1G, 1E, S1C, and S1D). Intestinal and body fat stores are also depleted upon genetic activation of PGRP-LE signaling, consistent with maldigestion (Figures 1H, 1J, and S1E). Finally, this manipulation reduces spontaneous locomotor activity, a hallmark of sickness behavior (Figure 1K).[20] Taken together, these data demonstrate that activation of PGRP-LE signaling in ECs induces maldigestion and malabsorption, has systemic repercussions on metabolism, and affects behavior.

PGRP-LE and PGRP-LC control intestinal metabolism with their cRHIM

The cRHIM is required for PGRP-LC and PGRP-LE to form an amyloid nucleus. This structure recruits other innate immune signaling components, leading to the activation of Rel/NF-κB.[11,12,14] To test whether the cRHIM is required for the regulation of intestinal metabolism by PGRP-LE, we overexpressed *PGRP-LE* and *PGRP-LE*$^{\Delta 14}$, a version of this PRR with a truncated cRHIM (Figure 2A).[11] Consistent with previous observations, a functional cRHIM is required for PGRP-LE to form cytoplasmic aggregates that get ubiquitinated and to induce Rel/NF-κB signaling (Figures 2B, 2C, S2A, and S2B).[12,14] The cRHIM is also required for PGRP-LE to alter the expression of digestive proteases, carbohydrases, and lipases and to reduce systemic lipid levels (Figures 2C–2E). We next sought to determine whether the same was true for PGRP-LC. To test this possibility, we overexpressed wild-type *PGRP-LCx* and a version of this PRR with a truncated cRHIM (*PGRP-LCx*$^{\Delta 14}$) (Figure S2C).[11] *PGRP-LCx* overexpression induces the Rel/NF-κB targets *DptA*, *pirk*, and *PGRP-SC1* in a cRHIM-dependent manner (Figure S2D). As seen previously with PGRP-LE, PGRP-LCx represses the expression of several proteases, carbohydrases, and lipases, and these effects are dependent on the presence of a functional cRHIM (Figures S2D and S2E). However, there are slight differences between the two PRRs: PGRP-LCx does not induce *Jon44E*, *Jon66ci*, *Jon66cii*, or *Jon74E* (encoding

(I and J) Bodipy stains were performed in (I) intestines and (J) dorsal abdomen containing adipose tissue to visualize neutral lipids. Scale bars: (I) 10 μm and (J) 200 μm. Tissues were counterstained with DAPI to visualize DNA. In (I), a representative image of R4 (posterior midgut) is shown.

(K) Spontaneous locomotor activity was scored using DAM2 *Drosophila* activity monitors. Graphs represent the average number of infrared beam breaks per day for individual animals. *mex*>+: $n = 35$ animals (15 animals censored), *mex*>*PGRP-LE*: $n = 42$ animals (8 animals censored).

(B–F, H, and K) Dots: individual biological replicates, midguts, or animals; horizontal line in the box plot: median; whiskers: minimum and maximum values. Data are from three independent experiments. $^{****}p \leq 0.0001$; $0.0001 < {}^{***}p \leq 0.001$; $0.001 < {}^{**}p \leq 0.01$; $0.01 < {}^{*}p \leq 0.05$ (Mann-Whitney test). See also Table S6.

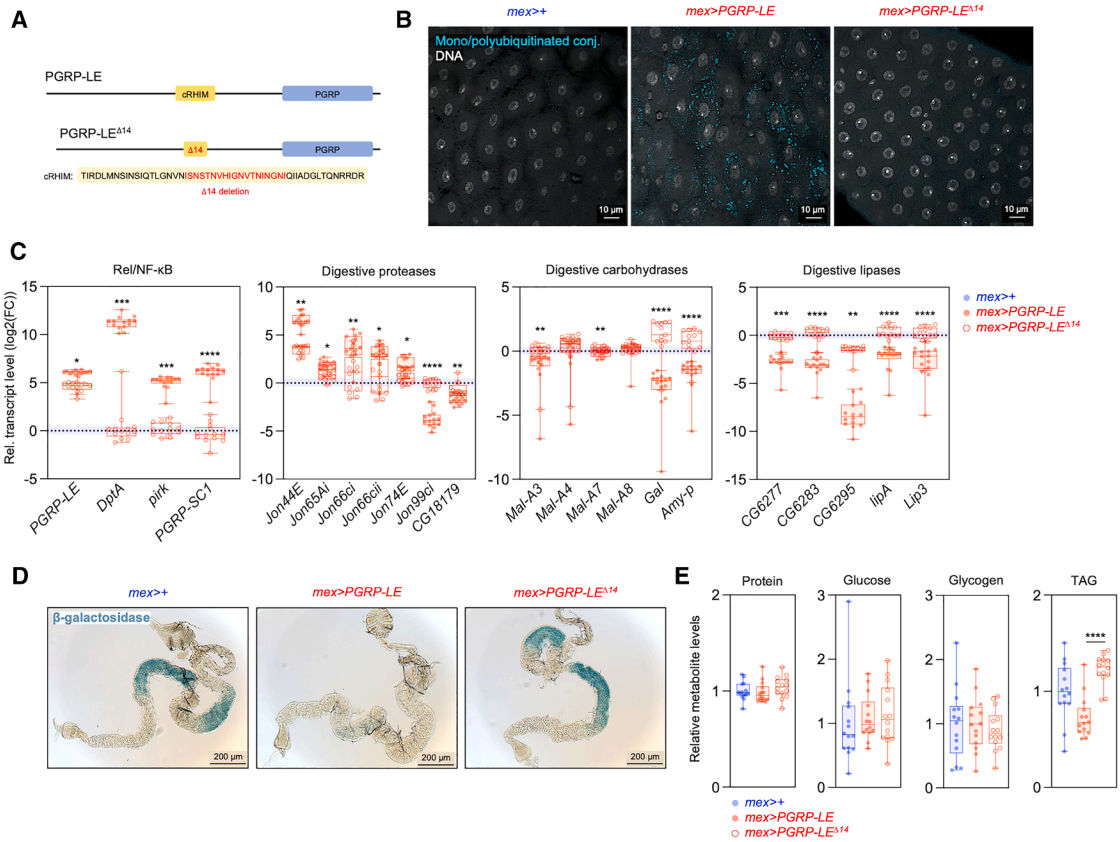

Figure 2. The cRHIM is required for PGRP-LE to suppress EC metabolism

(A) Schematic of full-length PGRP-LE and PGRP-LE$^{\Delta 14}$, a version of the receptor with a deletion in the cRHIM. The peptidoglycan recognition protein (PGRP) domain, the amino acid sequence of the cRHIM, and the Δ14 deletion are indicated.

(B–E) The two versions of the receptor were overexpressed in ECs by driving their expression with the *mex-GAL4* driver (*mex>PGRP-LE* and *mex>PGRP-LE*$^{\Delta 14}$, respectively).

(B) Antibodies against mono/polyubiquitinated conjugates were used to stain midguts. DAPI labels DNA. A representative view with a focal plane near the basal surface of ECs is shown. See also Figures S2A and S2B. Scale bar: 10 μm.

(C) The levels of representative transcripts regulated by Rel/NF-κB or encoding digestive proteases, carbohydrases, and lipases were scored by RT-qPCR in intestines. Graphs represent log2(FC) in transcript levels relative to *mex*>+ controls. Control values are not shown for clarity but are represented by a blue dotted line. 14 > n > 13 biological replicates.

(D) X-gal stains were used to visualize brush border β-galactosidase activity in the intestine. Scale bar: 200 μm.

(E) Protein, glucose, glycogen, and TAG levels were scored in whole animals. Metabolite levels were normalized to proteins and are presented relative to controls. n = 14 biological replicates.

(C and E) Dots: biological replicates; horizontal line in the box plot: median; whiskers: minimum and maximum values. Data from three independent experiments. Asterisks indicate statistically significant differences between (C) the *mex>PGRP-LE* and *mex>PGRP-LE*$^{\Delta 14}$ genotypes and (E) between the indicated genotypes (Dunn's multiple comparison test). ****$p \leq 0.0001$; $0.0001 <$ ***$p \leq 0.001$; $0.001 <$ **$p \leq 0.01$; $0.01 <$ *$p \leq 0.05$. See also Table S6.

proteases) and does not repress *Mal-A3*, *Amy-p*, or *Lip3* (encoding two carbohydrases and a lipase) (Figure S2D). Consistent with its overall effect on digestive enzymes, *PGRP-LCx* overexpression reduces whole-body TAG, and this effect depends on a functional cRHIM (Figure S2F). Taken together, these observations demonstrate that PGRP-LE and PGRP-LC regulate intestinal function and that these effects require a functional cRHIM.

PGRP-LE acts independently of Rel/NF-κB to suppress intestinal metabolism

Given that the cRHIM is required for PGRP-LE and PGRP-LC to exert their effects on metabolism, we wondered whether these regulations are also dependent on Rel/NF-κB signaling. To test this hypothesis, we overexpressed *PGRP-LE* while simultaneously blocking Rel/NF-κB activation. We used a loss-of-function mutation in *Dredd*, which encodes a caspase required for the activation of Rel/NF-κB downstream of PRRs (Figure 1A). Consistent with these regulatory relationships, *PGRP-LE* overexpression in a *Dredd* mutant background fails to induce *DptA*, *pirk*, and *PGRP-SC1* and EC apoptosis (Figures 3A and S3A; Table S6). However, it still induces intestinal stem cell mitoses, demonstrating that this effect is independent of Rel/NF-κB signaling (Figure S3B). In addition, most transcripts encoding digestive enzymes are still up- or downregulated following *PGRP-LE* overexpression in a *Dredd* mutant background, with

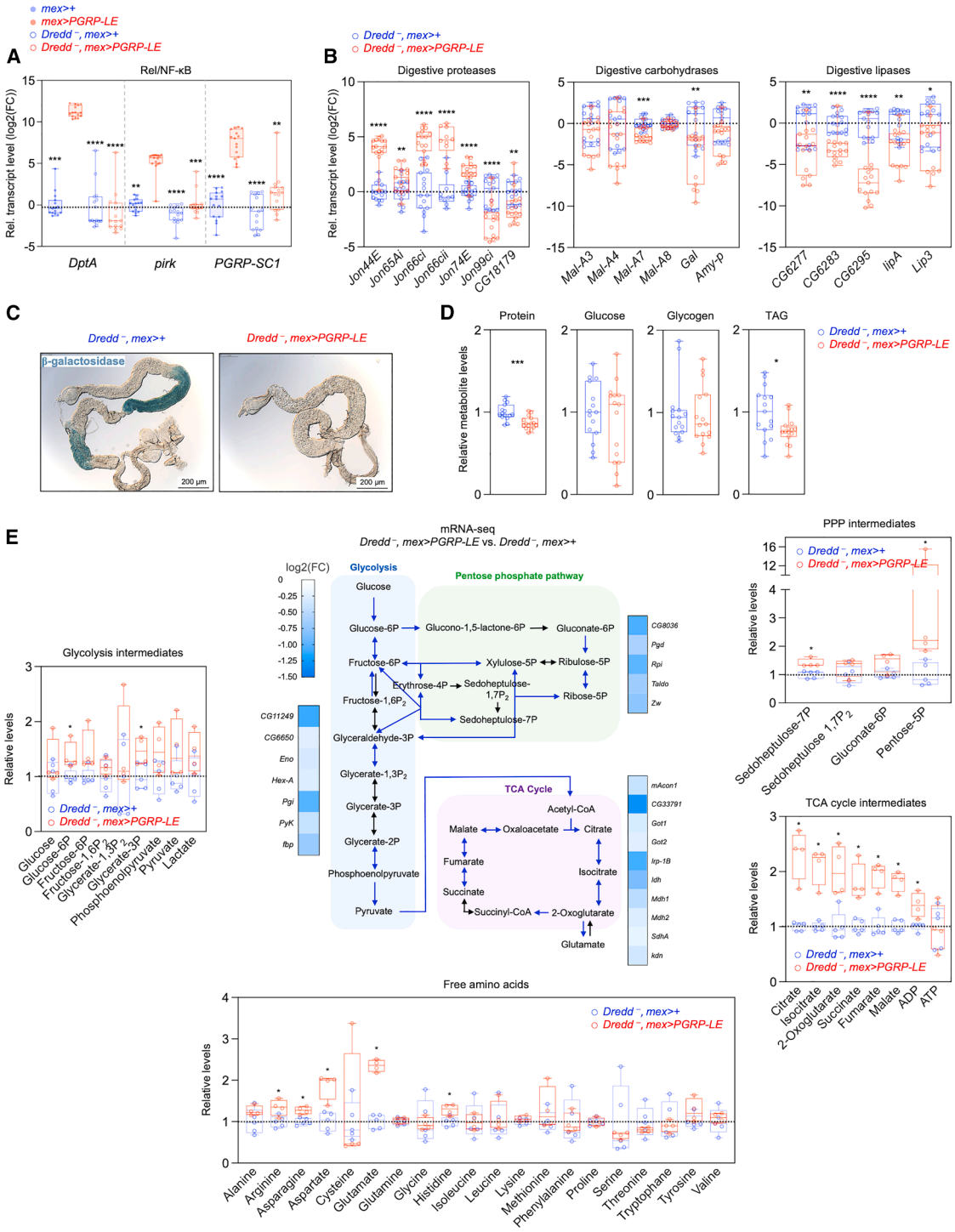

Figure 3. PGRP-LE acts independently of Dredd to suppress EC metabolism

(A–E) *PGRP-LE* was overexpressed in ECs (*mex>PGRP-LE*) in an otherwise wild-type or *Dredd* mutant background (*Dredd* $^{-}$).

(A and B) The levels of representative transcripts (A) regulated by Rel/NF-κB and (B) encoding digestive proteases, carbohydrases, and lipases were scored in the intestine by RT-qPCR. $15 > n > 10$ biological replicates; data are from three independent experiments. Graphs represent log2(FC) in transcript levels relative to (A) *mex>+* or (B) *Dredd* $^{-}$*, mex>+* controls.

(C) X-gal stains were used to visualize brush border β-galactosidase activity in intestines. Scale bar: 200 μm.

(D) Protein, glucose, glycogen, and TAG levels were scored in whole animals. Metabolite levels are normalized to protein content and shown relative to *Dredd* mutant controls. $n = 15$ biological replicates; data are from three independent experiments.

(legend continued on next page)

only few exceptions (Figure 3B). PGRP-LE also acts independently of Dredd to inhibit intestinal β-galactosidase activity, deplete fat stores, and reduce locomotor activity (Figures 3C, 3D, and S3C). Therefore, PGRP-LE acts largely independently of Rel/NF-κB to influence intestinal metabolism. Consistent with these observations, the overexpression of an activated form of Rel/NF-κB (Rel.68) induces *DptA*, *pirk*, and *PGRP-SC1* but suppresses *Jon65Ai*, while this protease is induced by both PGRP-LE and PGRP-LC (Figures S3D and S3E). Similarly, Rel.68 has no impact on the expression of *CG18179* and intestinal β-galactosidase activity, while both are strongly reduced by PGRP-LC and PGRP-LE (Figures S3E, S3F, 2C, 2D, S2D, and S2E). However, Rel.68 suppresses the expression of lipases, suggesting that PGRP-LC and PGRP-LE act through both Rel-dependent and -independent mechanisms to regulate these enzymes (Figure S3E). To support these findings and identify additional processes that could be regulated by PGRP-LE in a *Dredd*-independent manner, we performed mRNA sequencing (mRNA-seq) in *Dredd* mutant midguts with or without *PGRP-LE* overexpression in ECs (Table S1). These analyses confirmed our previous observations on transcripts encoding digestive enzymes (Figure S4A). Functional enrichment analysis of transcripts significantly downregulated in *PGRP-LE* intestines shows an over-representation of gene ontology terms related to EC function, including nutrient digestion, absorption, and metabolism (Figures S4B and S4C). In particular, numerous transcripts encoding steps in glycolysis, the pentose phosphate pathway, and the tricarboxylic acid cycle (hereafter collectively referred to as central carbon metabolism [CCM]) are reduced (Figures 3E and S4C). PGRP-LE acts independently of Dredd to suppress these transcripts, but the cRHIM is required for this effect (Figure S4D). To determine whether the transcriptional downregulation of CCM translates into metabolic changes, we performed metabolomics on midguts. We used germ-free animals to eliminate the influence of gut bacteria on metabolite levels (Table S2). Several intermediates of glycolysis, the pentose phosphate pathway, and the tricarboxylic acid cycle accumulate in *Dredd* mutant midguts overexpressing *PGRP-LE* (Figure 3E). This effect is particularly pronounced for the tricarboxylic acid cycle, with all intermediates and ADP being increased, except ATP (Figure 3E). This pattern suggests reduced mitochondrial metabolism, a hypothesis that is further supported by the marked accumulation of the anaplerotic amino acids glutamate and aspartate, while the levels of other amino acids are globally unchanged (Figure 3E). Therefore, transcriptomics and metabolomics support that defects in CCM occur in midguts overexpressing *PGRP-LE*. Taken together, our genetic, transcriptomic, and metabolomic analyses demonstrate that PGRP-LE regulates fundamental aspects of EC metabolism independently of the Dredd-Rel/NF-κB signaling axis.

PGRP-LE suppresses digestive lipase expression by inhibiting GATAe

To identify the transcription factors (TFs) that suppress EC metabolism downstream of PRRs, we scored for the enrichment of TF binding sites in the vicinity of genes whose expression is reduced when *PGRP-LE* is overexpressed in *Dredd* mutant ECs (Table S3). These analyses revealed an over-representation of binding sites for several members of the GATA family of TFs, including GATAe, a master regulator of EC identity.[21–23] Consistent with the suppression of *GATAe* expression after oral infection,[19] PGRP-LE reduces GATAe levels in EC nuclei, and this effect requires a functional cRHIM (Figure 4A). In parallel, silencing *GATAe* in ECs has broad, negative impacts on digestive proteases, carbohydrases, and lipases but also suppresses transcripts involved in CCM (Figures 4B–4E). These observations suggest that PGRP-LE represses a subset of metabolic activities in ECs by inhibiting GATAe. Therefore, we aimed to restore *GATAe* levels in *PGRP-LE*-overexpressing ECs. We simultaneously expressed *PGRP-LE* and *GATAe* in ECs and scored the expression of transcripts encoding digestive enzymes (Figure 4F). These two transgenes were induced for 48 h because we observed lethality with chronic *GATAe* expression in ECs. Co-expression of *GATAe* with *PGRP-LE* has no impact on carbohydrases, except for a further reduction of *Mal-A8* levels (Figure 4F). In contrast, *Jon74E* transcript levels are significantly increased under this condition (Figure 4F). Thus, GATAe could be limiting for the full induction of this protease under *PGRP-LE* overexpression. In addition, co-expression of *GATAe* with *PGRP-LE* rescues the expression of the lipases *CG6283* and *Lip3* and increases the levels of *CG6277*, *CG6295*, and *lipA*, although the latter changes are not statistically significant (Figure 4F). Taken together, these data demonstrate that PGRP-LE regulates the expression of lipases and the *Jon74E* protease, at least in part, by inhibiting GATAe.

PGRP-LE acts through ERK to induce a set of digestive proteases

Given that PGRP-LE induces maldigestion and malnutrition, this PRR could suppress nutrient-sensing pathways. To test this hypothesis, we scored Foxo nuclear levels and 4E-BP phosphorylation as indicators of phosphatidylinositol 3-kinase (PI3K)/Akt signaling activity in midguts. While Foxo levels are generally increased under *PGRP-LE* overexpression, nuclear Foxo is

(E) mRNA-seq and metabolomics analyses were performed in *Dredd* mutant intestines (*Dredd* $^{-}$*, mex*>+) and *Dredd* mutant intestines with *PGRP-LE* overexpression in ECs (*Dredd* $^{-}$*, mex*>*PGRP-LE*). The schematic shows central carbon metabolism (CCM). Steps in glycolysis, the pentose phosphate pathway (PPP), and tricarboxylic acid (TCA) cycle whose respective transcripts are significantly downregulated in *Dredd* $^{-}$*, mex*>*PGRP-LE* intestines are marked in blue. Transcript levels are also shown in heatmaps. $n = 5$ biological replicates. See also Table S1. Dot plots show levels of glycolysis, PPP, and TCA cycle intermediates as well as free amino acids in the midgut, as determined by metabolomics. "Pentose-5P″ corresponds to a pentose phosphate class containing ribose-5-P and ribulose-5-P; pentose phosphates could not be further distinguished. Metabolite levels are normalized to the total protein content of midgut homogenates and are shown relative to *Dredd* $^{-}$*, mex*>+ control midguts. $n = 5$ biological replicates for *Dredd* $^{-}$*, mex*>+ controls, and $n = 4$ biological replicates for *Dredd* $^{-}$*, mex*>*PGRP-LE*. See also Table S2.

(A, B, D, and E) Dots: biological replicates; horizontal line in the box plot: median; whiskers: minimum and maximum values. Asterisks indicate statistically significant differences from (A) *mex*>*PGRP-LE* (Dunn's multiple comparison test) and (B, D, and E) *Dredd* $^{-}$*, mex*>+ (Mann-Whitney test). ****$p \leq 0.0001$; 0.0001 < ***$p \leq 0.001$; 0.001 < **$p \leq 0.01$; 0.01 < *$p \leq 0.05$. See also Table S6.

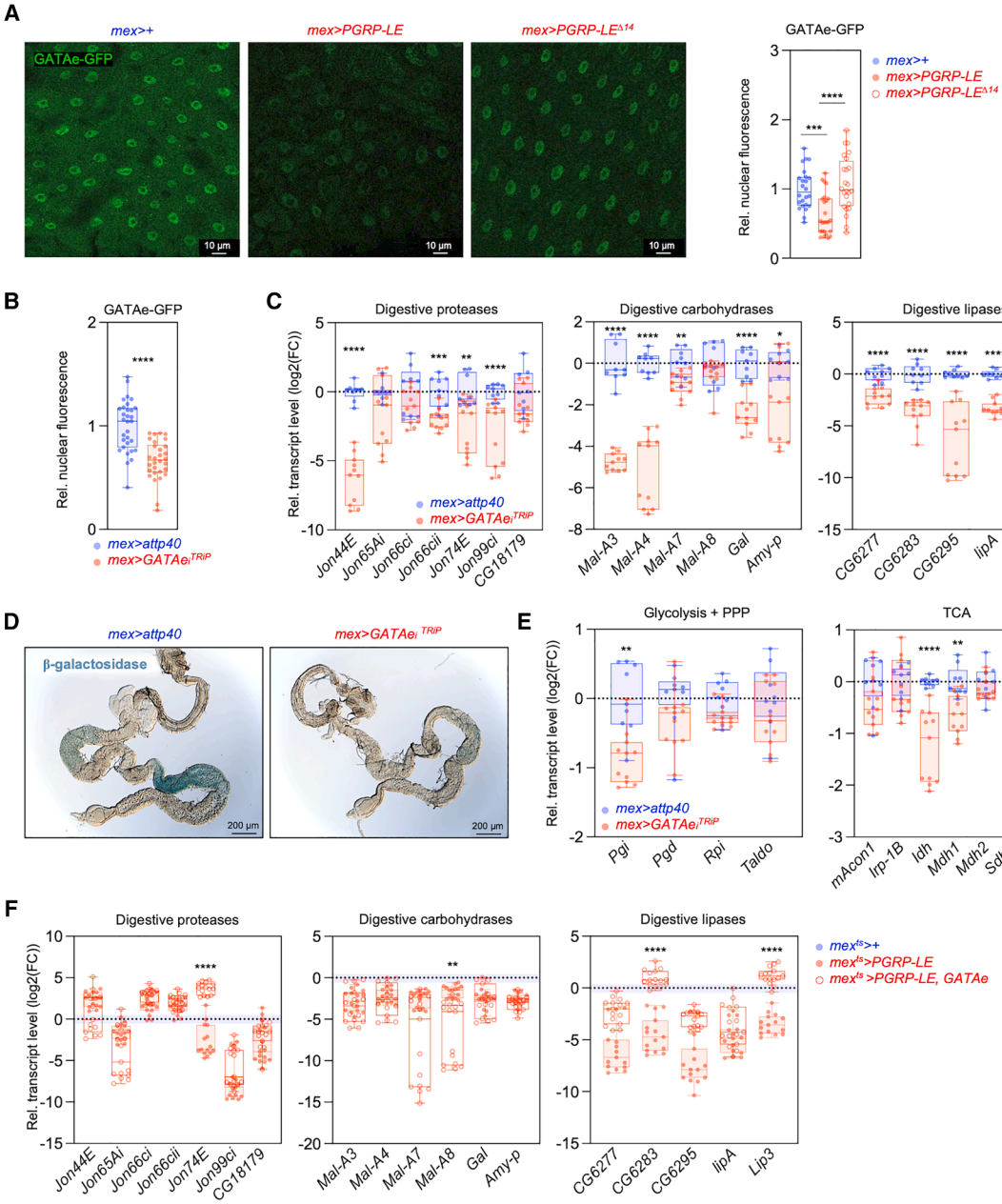

Figure 4. PGRP-LE inhibits GATAe, a master regulator of EC function

(A and B) A *GATAe-GFP* transgene was used to quantify nuclear GATAe levels following expression of (A) *UAS-PGRP-LE* and *UAS-PGRP-LE*$^{\Delta 14}$ and (B) *UAS-GATAe* RNAi in ECs (*mex>PGRP-LE, mex>PGRP-LE* $^{\Delta 14}$, and *mex>GATAe*$_i^{TRiP}$, respectively).

(A) Scale bar: 10 µm.

(A and B) Graphs show quantifications in R2 (anterior midgut), data are presented relative to control levels. 31 > *n* > 24 midguts.

(C and E) The levels of representative transcripts encoding (C) digestive proteases, carbohydrases, and lipases and (E) steps in CCM were scored by RT-qPCR in intestines. Graphs represent log2(FC) in transcript levels relative to *mex>attp40* controls. 11 > *n* > 9 biological replicates.

(D) X-gal stains were used to visualize brush border β-galactosidase activity in the intestine. Scale bar: 200 µm.

(F) The *mex-GAL4* and *tub-GAL80*^{ts} transgenes (*mex*^{ts}) were used to express *UAS-PGRP-LE* and *UAS-GATAe* alone or in combination in ECs of 7-day-old adult males for 48 h. The levels of representative transcripts encoding digestive proteases, carbohydrases, and lipases were scored by RT-qPCR in whole flies. Graphs represent log2(FC) in transcript levels relative to *mex*^{ts}>+ controls. Control values are not shown for clarity but are represented by a blue dotted line. *n* = 15 biological replicates.

(legend continued on next page)

reduced (Figure 5A). This suggests translocation of Foxo out of the nucleus and inhibition of its activity, contrary to our initial hypothesis. 4E-BP phosphorylation, an indicator of TOR activation, is also increased under this condition (Figure 5B). Consistent with these observations, autophagy is reduced, and various ubiquitinated proteins accumulate in *PGRP-LE*-overexpressing midguts (Figures S5A–S5D).[24] Therefore, PGRP-LE could activate PI3K/Akt signaling despite maldigestion. Since these effects are unlikely explained by increased insulin levels, we sought to identify the mechanisms involved. PI3K is regulated by several receptor tyrosine kinases, including the epidermal growth factor receptor (EGFR)[25] (Figure 5C). *PGRP-LE* overexpression induces a marked accumulation of EGFR in *Dredd* mutant ECs (Figure 5D). EGFR regulates PI3K activity but also extracellular signal-regulated kinase (ERK) signaling (Figure 5C). Consistent with increased EGFR levels, the activated, phosphorylated form of ERK (p-ERK) accumulates in ECs overexpressing *PGRP-LE* (Figure 5E). p-ERK levels are still increased, although not significantly, when *PGRP-LE* is overexpressed in *Dredd* mutant ECs (Figure 5F). Therefore, Rel/NF-κB is not essential for PGRP-LE to activate ERK. Since ERK regulates several cell functions,[26] we studied the functional consequences of its activation following *PGRP-LE* overexpression. For this, we treated animals with trametinib, an inhibitor of the mitogen-activated protein kinase/ERK kinase (MEK/Dsor1) (Figure 5C). Trametinib feeding effectively reduces p-ERK levels following *PGRP-LE* overexpression in ECs (Figure S5E). This treatment does not affect transcripts encoding lipases, carbohydrases, or CCM enzymes following *PGRP-LE* overexpression in *Dredd* mutant ECs (Figure S5F). However, trametinib significantly attenuates the induction of *Jon65Ai* and *Jon66ci* and reduces *Jon66cii* and *Jon74E* transcripts levels, although the latter effect is not statistically significant (Figure 5G). Taken together, our observations show that ERK acts downstream of PGRP-LE to induce several digestive proteases. From a broader perspective, our studies of GATAe and ERK indicate that PGRP-LE acts through multiple pathways to regulate different classes of digestive enzymes.

PGRP-LE affects luminal bacteria in a *Dredd*-independent manner

Gavage with *Pseudomonas entomophila* rapidly induces PRR signaling and has widespread, negative effects on intestinal function in control animals (Figures S6A–S6C).[15,27,28] In contrast, monoassociation of germ-free controls with a gram-negative enterobacterium induces chronic, low-grade PRR signaling and does not affect gut function (Figure S6D). Therefore, gut metabolic remodeling may occur after ingestion of food heavily contaminated with bacteria to prevent infection. In particular, this metabolic response may control bacteria in the lumen; loss of digestion could affect microorganisms that depend on their hosts for nutrient extraction. To test this possibility, we analyzed microbiome diversity in conventionally reared *Dredd* mutants with *PGRP-LE* overexpression in ECs (Figure 6A). There is no induction of the immune response under this genetic condition, allowing us to directly study the effect of intestinal metabolic remodeling on luminal bacteria. In *Dredd* mutants, the composition of the microbiome is relatively simple, with eight dominant genera. However, there is great variation between replicates; microbiomes contain one to four genera, the most abundant being *Acetobacter*, *Lactiplantibacillus*, *Levilactobacillus*, *Paracoccus*, and *Staphylococcus*. In contrast, *Lactiplantibacillus* dominates (with a relative abundance above 50%) in six of seven replicates in *Dredd* mutants with *PGRP-LE* overexpression in ECs. Consistent with these observations, Shannon and Simpson indices, which summarize alpha diversity, show greater variability in *Dredd* mutants than in *Dredd* mutants with *PGRP-LE* overexpression in ECs (Figure 6B). However, there is no significant difference between genotypes (p = 0.5360 and 0.4698 for Shannon and Simpson indices, respectively; Figure 6B). The two genotypes also do not segregate on principal-coordinate analysis plots of unweighted UniFrac distances, a measure of beta diversity (PERMANOVA, p = 0.122; Figure 6C). Although there is no significant difference in diversity, these data suggest that PGRP-LE promotes *Lactiplantibacillus* at the expense of other commensals. In agreement with this hypothesis, qPCR on genomic DNA extracted from whole flies indicates that *PGRP-LE* overexpression leads to a non-significant increase in *Lactiplantibacillus* (p = 0.0753), while total bacterial density is unaffected (Figure 6D). In parallel, we quantified live lactobacilli in midguts by plating tissue homogenates on De Man, Rogosa, and Sharpe (MRS) agar, a selective medium for lactic acid bacteria (Figure 6E). *PGRP-LE* overexpression in *Dredd* mutant intestines leads to a marked increase in lactic acid bacteria, further supporting a model in which PRR-driven gut metabolic remodeling favors the dominance of *Lactiplantibacillus*. Taken together, these data demonstrate the PRR-driven gut metabolic remodeling channels microbiome composition.

PRRs suppress gut function to control parasitic endosymbionts

In addition to luminal bacteria, the *Drosophila* midgut can be colonized by endosymbionts. These microorganisms live intracellularly or in the body cavity of their hosts and, in most cases, depend on them for their metabolic needs. Intracellular endosymbionts of the genus *Wolbachia* infect up to half of all arthropod species, including *Drosophila*.[29–31] When *Dredd* mutants are infected with *Wolbachia*, this parasitic bacterium becomes predominant in the gut, accounting for 66% of all detected bacteria (Figures 7A and 7B).[32] *Wolbachia* reside in intracellular vacuoles, which may shield them from AMPs.[33] We therefore sought to determine whether PRR-driven gut metabolic remodeling suppresses the growth of these endosymbionts. Consistent with this hypothesis, *PGRP-LE* overexpression reduces intestinal *Wolbachia* load in a cRHIM-dependent but

(A–C, E, and F) Dots: individual midguts or biological replicates; horizontal line in the box plot: median; whiskers: minimum and maximum values. Data from three independent experiments. Asterisks indicate statistically significant differences (A) between genotypes (Dunn's multiple comparison test), (B, C, and E) with *mex>attp40* controls (Mann-Whitney test), and (F) between *mex^{ts}>PGRP-LE*, *mex^{ts}>PGRP-LE*, and *GATAe* (Dunn's multiple comparison test). ****$p \leq 0.0001$; $0.0001 <$ ***$p \leq 0.001$; $0.001 <$ **$p \leq 0.01$; $0.01 <$ *$p \leq 0.05$. See also Table S6.

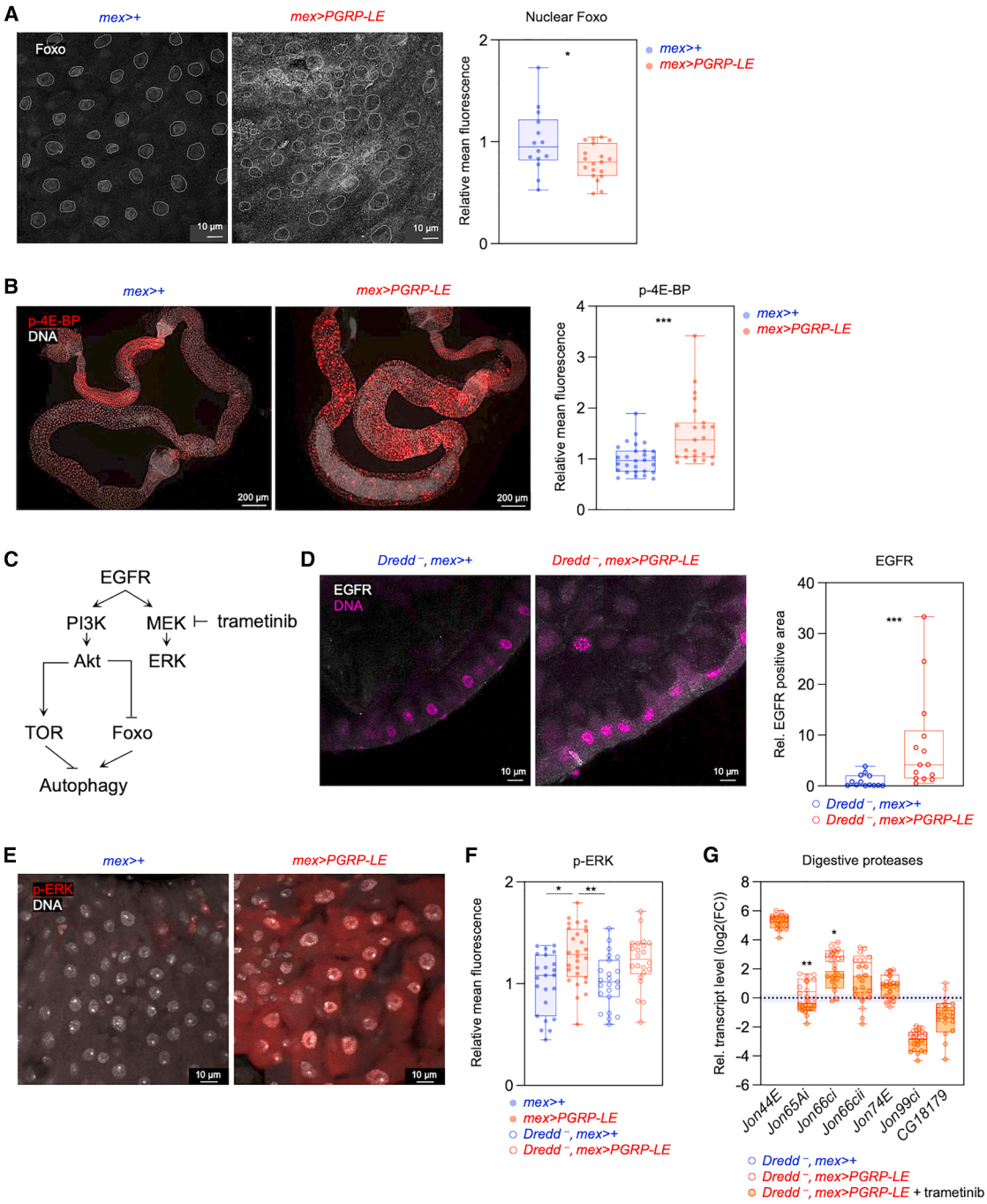

Figure 5. PGRP-LE acts through ERK to induce a set of digestive proteases

(A–G) *PGRP-LE* was overexpressed in ECs (*mex>PGRP-LE*) in an otherwise wild-type or *Dredd* mutant background (*Dredd* $^{-}$).

(A) Antibody stains were used to score Foxo nuclear levels in intestines. Left: representative frontal views of R2; nuclei are indicated by a dotted line. Right: quantification of nuclear fluorescence intensity in views of R2. 19 > *n* > 14 midguts. Scale bar: 10 µm.

(B) Antibody stains were used to score p-4E-BP levels in intestines. Right: quantification of fluorescence intensity in whole midguts. 28 > *n* > 23 midguts. Scale bar: 200 µm.

(A and B) Quantifications are presented relative to controls.

(C) Simplified representation of the regulation of TOR, Foxo, and autophagy by EGFR and of ERK inhibition by trametinib.

(D) Antibody stains were used to score EGFR levels in intestines. Intestines were counterstained with DAPI to visualize DNA. Left: transverse views of R2 (anterior midgut). Right: quantification of EGFR-positive areas in confocal images. Quantifications are presented relative to control levels. 14 > *n* > 13 midguts. Scale bar: 10 µm.

(legend continued on next page)

Dredd-independent manner (Figures 7C and S7A). In parallel, enteric infection with *P. entomophila* reduces *Wolbachia* load in control intestines, further supporting the theory that gut metabolic remodeling controls endosymbionts (Figure S7B). We also observed that *PGRP-LE* overexpression in ECs reduces systemic *Wolbachia* titer, suggesting non-autonomous effects on endosymbionts (Figure S7C). Accordingly, *PGRP-LE* overexpression in ECs reduces *Wolbachia* load in the ovary, an organ normally heavily colonized by these endosymbionts[32,34] (Figure 7D). We next sought to determine which metabolic activities are limiting for *Wolbachia* growth under *PGRP-LE* overexpression. PGRP-LE suppresses digestive lipase expression by inhibiting GATAe (Figures 4A–4E). In parallel, *GATAe* RNAi dramatically reduces *Wolbachia* load in the midgut, suggesting that fat digestion is limiting for endosymbiont infection, consistent with the reliance of these microorganisms on host-derived lipids[35,36] (Figures S7D). *GATAe* RNAi also affects CCM, and this pathway could also control endosymbionts; it provides metabolic precursors, energy, and reducing agents necessary for lipid synthesis (Figure 4E). To test this possibility, we inhibited CCM independently of PRR and GATAe by silencing the estrogen-related receptor (ERR), a major transcriptional activator of this pathway (Figure 7E).[37,38] Silencing *ERR* in ECs reduces both intestinal and ovarian *Wolbachia* loads, demonstrating that intestinal CCM controls endosymbionts at the local and systemic level (Figures 7F and 7G). Taken together, these observations support a model in which PRRs act independently of Rel/NF-κB to suppress digestion and CCM in the intestine. This metabolic response limits endosymbionts in the gut and in peripheral tissues, likely by imposing nutrient restriction on these microorganisms. More broadly, our observations support the model that PRRs use distinct pathways to drive antimicrobial and metabolic responses in the gut to control specific classes of microbes.

DISCUSSION

Non-canonical signaling downstream of PRRs controls intestinal function

Since the discovery of the first *Drosophila* PRR in the early 2000s, these receptors have been extensively studied for their role in the regulation of the immune response.[39] This regulation involves a canonical signaling cascade leading to the activation of NF-κB and the production of AMPs. However, PGRP-LE can suppress the proliferation of intracellular *Listeria*[40] and *Wolbachia* independently of Rel/NF-κB signaling and, thus, AMPs (Figure 7C). Based on our findings, we propose that PRRs alter metabolism in order to complement the immune response. This metabolic response may be particularly efficient for controlling intracellular bacteria, which are difficult to reach by AMPs. The mechanisms linking PRRs to metabolism remain to be fully elucidated, but we can formulate several hypotheses based on our findings. The cRHIM is required for PGRP-LE, PGRP-LC, and the adaptor Imd to form signaling amyloids, which recruit effector enzymes that activate Rel/NF-κB[11,12,14] (Figures 2C and S2D). The cRHIM is also required for PGRP-LE and PGRP-LC to repress intestinal metabolism (Figures 2C, 2D, S2D, and S2E). Thus, PRR amyloids could recruit both immune and metabolic regulators. Consistent with this hypothesis, hundreds of proteins interact with canonical members of the Imd pathway.[41] Our data show that GATAe acts downstream of PGRP-LE to control the expression of lipases (Figure 4F). The transcriptional activity of the GATA family of TFs is regulated by post-translational modifications and protein-protein interactions in mammals.[42] Therefore, PRR amyloids could suppress EC function via post-transcriptional modification of GATAe or by sequestering it away from the nucleus (Figure 4A).[42] In parallel, enteric infection leads to the formation of PGRP-LE aggregates that colocalize with endosomes.[43] PRR amyloids could therefore influence endosome trafficking and, thus, the internalization, recycling, and degradation of membrane receptors, such as EGFR. This would explain why EGFR accumulates in *PGRP-LE* overexpressing ECs, leading to the activation of ERK and the induction of proteases (Figures 5D–5G). Finally, PGRP-LE inhibits autophagy in the gut, which may further stabilize amyloids and prolong signaling by these complexes (Figure S5A).

Suppression of intestinal function as a defense mechanism against bacteria

Loss of brush border disaccharidases and malabsorption are often observed after gastrointestinal infection or during small intestinal bacterial overgrowth, a condition characterized by abnormally high bacterial density in the small intestine.[44–48] These defects are often attributed to epithelial damage. Our data suggest an alternative hypothesis: PRRs actively suppress gut function to limit bacterial access to nutrients. We propose that this metabolic response works in concert with sickness behavior, a set of behavioral changes that occur in infected animals to complement the immune response.[20] Specifically, sickness behavior includes loss of appetite, which could act synergistically with suppression of digestion to further limit nutrient availability for bacteria.[20] Therefore, the combination of immune, metabolic, and behavioral responses may maximize the chance of clearing an infection by attacking microorganisms on multiple fronts. However, this strategy is costly, as it creates metabolic vulnerabilities in hosts (Figures 1H, 3D, and S2F). Our

(E and F) Antibody stains were used to score p-ERK levels in intestines.
(E) Representative view of R2. Scale bar: 10 μm.
(F) Quantification of fluorescent signal in whole midguts. Quantifications are presented as relative to control levels. $28 > n > 22$ midguts.
(G) The levels of representative transcripts encoding digestive proteases were scored by RT-qPCR in *Dredd* mutant intestines with *PGRP-LE* overexpression in ECs and with or without trametinib treatment. Graph represents log2(FC) in transcript levels relative to untreated *Dredd*$^{-}$, *mex*>+ controls. Control values are not shown for clarity but are represented by a blue dotted line. $14 > n > 13$ biological replicates (see also Figures S5E and S5F).
(A, B, D, F, and G) Dots: individual midguts or biological replicates; horizontal line in the box plot: median; whiskers: minimum and maximum values. Data are from (A) two or (B, D, F, and G) three independent experiments. Asterisks indicate statistically significant differences: (A, B, and D) with *mex*>+ controls (Mann-Whitney test), (F) between genotypes (Dunn's multiple comparison test), and (G) between untreated and treated *Dredd*$^{-}$, *mex*>*PGRP-LE* intestines (Dunn's multiple comparison test). $0.0001 < ***p \leq 0.001$; $0.001 < **p \leq 0.01$; $0.01 < *p \leq 0.05$. See also Table S6.

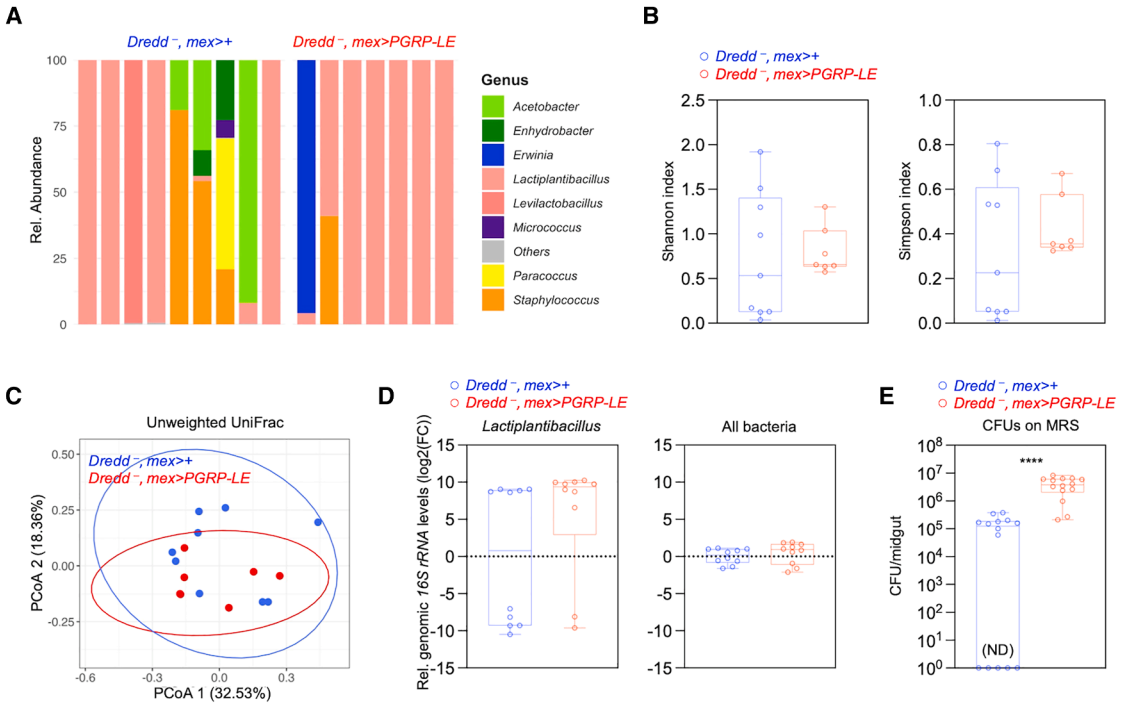

Figure 6. PGRP-LE affects luminal bacteria in a Dredd-independent manner

(A–C) *16S rRNA* amplicon sequencing was performed on gut genomic DNA to determine microbiome composition in *Dredd* mutants (*Dredd*$^{-}$, *mex*>+) and *Dredd* mutants with *PGRP-LE* expression in ECs (*Dredd*$^{-}$, *mex*>*PGRP-LE*). For these experiments, animals were fed a preservative-free diet because these xenobiotics limit gut bacterial density and diversity. n = 9 biological replicates for *Dredd*$^{-}$, *mex*>+, and 7 for *Dredd*$^{-}$, *mex*>*PGRP-LE*.

(A) Bar graphs represent the relative proportion of the most abundant bacterial genera in each biological replicate of the two genotypes. Genera whose abundance was less than 1% are grouped as "others".

(B) Comparison of microbiome alpha diversity in the two genotypes using Shannon-Wiener and Simpson diversity indices. Each dot represents one biological replicate.

(C) Principal-coordinate analysis (PCoA) plots of unweighted UniFrac distances of gut bacterial communities. Ellipses show 95% confidence intervals. Each dot represents a biological replicate. Note that two replicates overlap under the *Dredd*$^{-}$, *mex*>*PGRP-LE* condition.

(D) *Lactiplantibacillus* and total bacterial loads were scored by qPCR analysis of the *16S rRNA* genomic sequence in genomic DNA extracted from whole flies. n = 10 biological replicates; data are from two independent experiments. See also Table S6.

(E) Intestinal lactic acid bacteria were quantified by plating midgut homogenates on De Man, Rogosa, and Sharpe (MRS) nutrient agar. n = 14 individual midguts for each genotype. Data are from two independent experiments. CFU, colony-forming unit; ND, not detected. When no CFUs were detected, values were set to 1 for compatibility with the log10 scale.

(B, D, and E) Dots: individual midguts or biological replicates; horizontal line in the box plot: median; whiskers: minimum and maximum values. Asterisks indicate statistically significant differences between genotypes. ****$p \leq 0.0001$ (Mann-Whitney test).

data suggest that sickness behavior also originates in the gut. Indeed, activation of PRR signaling in ECs reduces spontaneous locomotor activity, recapitulating post-infectious lethargy (Figures 1K and S3C).[20] Further studies are needed to determine whether other components of sickness behavior, such as loss of appetite, are under intestinal control in *Drosophila*. Nevertheless, such regulatory relationships are consistent with the fact that the gut is often the first to come into contact with infectious microorganisms.

Finally, the gut microbiome can produce nutrients that are essential for metazoans, and intestinal bacteria have mostly been studied for their direct contributions to host nutrition. However, it is becoming increasingly clear that bacteria influence animal metabolism and physiology in ways that extend beyond the direct supply of nutrients. The mechanisms supporting these indirect effects remain largely unknown. Given the profound impact of PRR signaling on nutrient digestion and metabolism, these regulations open new perspectives on how gut bacteria and MAMPs influence nutrition, metabolism, and behavior in animals.[49]

Metabolic control of *Wolbachia*, an endosymbiont of public health interest

We used *Wolbachia* as model endosymbionts due to their ecological and public health relevance. *Wolbachia* have negative impacts on the reproductive success of their hosts but offer protection against the arthropod-borne viruses (arboviruses) responsible for dengue, chikungunya, Zika, and yellow fever.[29–31] This led the World Mosquito Program to test the large-scale release of *Wolbachia*-infected mosquitoes to control human arbovirus outbreaks.[31] How *Wolbachia* provide antiviral protection remains unclear, but these effects may originate in the midgut, a primary entry point for arboviruses.[50] Therefore, understanding *Wolbachia* biology in the insect midgut is of public health

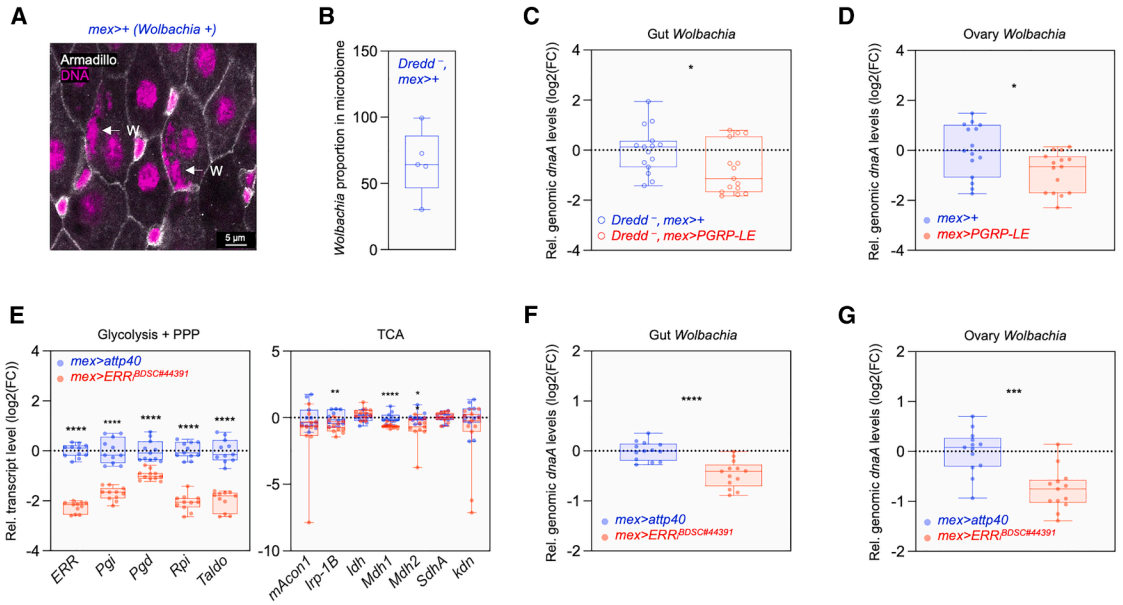

Figure 7. PRR signaling suppresses metabolism to control endosymbionts

(A) Representative view of R4 in a midgut infected with the intracellular bacterium *Wolbachia*. *Wolbachia* (W) are indicated with a white arrow and stained with DAPI, which labels cellular and bacterial DNA. Anti-Armadillo antibodies mark intercellular junctions. Scale bar: 5 µm.

(B) Proportion of *Wolbachia* in the microbiome of *Dredd* mutant intestines (*Dredd* $^{-}$*, mex>+*), as determined by *16S rRNA* bacterial profiling. $n = 5$ biological replicates. Animals were fed a preservative-free diet because these xenobiotics limit gut bacterial density and diversity.

(C, D, F, and G) Gut and ovarian *Wolbachia* loads were determined by qPCR analysis of the *Wolbachia dnaA* genomic sequence in genomic DNA extracted from tissues. $15 > n > 13$ biological replicates; data are from three independent experiments.

(E) The levels of representative transcripts encoding steps in CCM were scored by RT-qPCR in guts with *ERR* suppression in ECs (*mex>ERR*$_i^{BDSC\#44391}$). $n = 11$ biological replicates; data are from three independent experiments.

(B–G) Dots: biological replicates; horizontal line in the box plot: median; whiskers: minimum and maximum values.

(C–G) Graphs represent log2(FC) in genomic sequence or transcript levels relative to controls. Asterisks indicate statistically significant differences from controls. ****$p \leq 0.0001$; $0.0001 <$ ***$p \leq 0.001$; $0.001 <$ **$p \leq 0.01$; $0.01 <$ *$p \leq 0.05$ (Mann-Whitney test). See also Table S6.

interest. *Wolbachia* reside in intracellular vacuoles, which may shield them from AMPs.[33] Consistent with this, PGRP-LE reduces *Wolbachia* loads in the midgut independently of AMP production (Figure 7C). Our data support the theory that PRR-driven intestinal metabolic remodeling is required for this effect (Figures 7F, S7B, and S7D). The suppression of gut function also limits *Wolbachia* infection in the ovary (Figures 7D and 7G). This non-autonomous effect is particularly relevant for *Wolbachia* biology, as these endosymbionts are mostly transmitted vertically, through the female germline.[29,30] Future studies are needed to determine whether intestinal PGRP-LE/LC signaling and metabolic remodeling limit transgenerational *Wolbachia* transmission in *Drosophila* and whether similar effects are seen in mosquitoes. In parallel, tissue-specific studies in *Wolbachia-Drosophila* symbiosis may improve the use of this bacterium for arbovirus biocontrol.

From a broader perspective, our findings highlight complementary responses triggered by bacterial sensing pathways to contain infection. NF-κB-dependent AMP production targets free-living bacteria found in the gut lumen or in the circulation. On the other hand, NF-κB-independent gut metabolic remodeling controls intracellular endosymbionts that are otherwise difficult to reach by antimicrobials. Thus, our work uncovers a role for epithelial bacterial sensing in the control of endosymbionts that may be more broadly applicable to intracellular pathogens.

Limitations of the study

This study supports a model where PGRP-LC and PGRP-LE act through GATAe and ERK to regulate the expression of digestive lipases and proteases. However, how these factors are controlled by PRRs remains to be characterized. Similarly, how PGRP-LC and PGRP-LE inhibit carbohydrate digestion remains to be determined. Our data support the theory that PRR-driven intestinal metabolic remodeling controls endosymbionts. Whether this process also affects intracellular bacteria that do not live in obligate symbiosis with their hosts remains to be determined. Finally, these findings were made using overexpression models and enteric infection with concentrated bacterial inocula. The impact of these regulations on the physiology and fitness of *Drosophila* under more natural conditions will need further investigation.

RESOURCE AVAILABILITY

Lead contact

Requests for further information, resources, and reagents should be directed to and will be fulfilled by the lead contact, Gilles Storelli (gilles.storelli@cos.uni-heidelberg.de).

Materials availability

All unique/stable reagents generated in this study are available from the lead contact with a completed materials transfer agreement.

Data and code availability

- RNA-seq data have been deposited at GEO (GEO: GSE278928). *16S rRNA* sequencing data have been deposited at SRA (SRA: PRJNA1256711). Metabolomics and lipidomics data have been deposited at Zenodo (Zenodo: 15303437, 15311025). Data will be publicly available as of the date of publication. Accession numbers are also listed in the key resources table.
- This paper does not report original code.
- Any additional information required to reanalyze the data reported in this paper is available from the lead contact upon request.

ACKNOWLEDGMENTS

The authors thank FlyBase,[51] the Vienna *Drosophila* Resource Center (VDRC; Vienna, Austria), the Bloomington Drosophila Stock Center supported by the NIH (NIH P40OD018537) (BDSC; Bloomington, IN, USA), the Transgenic RNAi Project (TRiP), the Developmental Studies Hybridoma Bank (DSHB; Iowa City, IA, USA), and the *Drosophila* Genomics Resource Center supported by the NIH (2P40OD010949) (DGRC; Bloomington, IN, USA). The authors also thank B.A. Edgar, T. Hoppe, N. Kremer, B. Lemaitre, F. Leulier, J. Mattila, I. Miguel-Aliaga, N. Silverman, and A. Wodarz for sharing reagents; J. Pleinis for assistance with *Drosophila* activity monitors; C. Lefranc for assistance with bioinformatics analyses; M.C. Vonolfen for assistance with microscopy analyses; B. Collins for fly transgenesis; R. Muny, S. Brodesser, and the CECAD lipidomics/metabolomics facility, the CECAD imaging facility, and the Cologne Center for Genomics for technical support; and the Storelli lab members and F. Leulier for their comments on the manuscript. This work is supported by ERC grant METABIONT, project number 101075974 (https://doi.org/10.3030/101075974) (to G.S.). This work was funded by the European Union. Views and opinions expressed are however those of the author(s) only and do not necessarily reflect those of the European Union or the European Research Council Executive Agency. Neither the European Union nor the granting authority can be held responsible for them. This work was also funded by the Deutsche Forschungsgemeinschaft (DFG, German Research Foundation) under Germany's Excellence Strategy EXC 2030-390661388 (to G.S.).

AUTHOR CONTRIBUTIONS

G.S. supervised the work. G.S. and S.B. designed and interpreted experiments with input from M.U. and F.L.M.z.A. G.S., S.B., F.L.M.z.A., H.J.L., and D.V. performed experiments. P.G. performed the metabolomics analysis. A. G. performed the transcriptomics analysis. A.F. performed the microbiome analysis. G.S. and S.B. wrote the paper.

DECLARATION OF INTERESTS

The authors declare no competing interests.

STAR★METHODS

Detailed methods are provided in the online version of this paper and include the following:

SUPPLEMENTAL INFORMATION

Supplemental information can be found online at https://doi.org/10.1016/j.celrep.2025.115811.

Received: November 21, 2024
Revised: April 16, 2025
Accepted: May 19, 2025
Published: June 6, 2025

REFERENCES

1. McFall-Ngai, M., Hadfield, M.G., Bosch, T.C.G., Carey, H.V., Domazet-Lošo, T., Douglas, A.E., Dubilier, N., Eberl, G., Fukami, T., Gilbert, S.F., et al. (2013). Animals in a bacterial world, a new imperative for the life sciences. Proc. Natl. Acad. Sci. USA *110*, 3229–3236. https://doi.org/10.1073/pnas.1218525110.
2. Pradeu, T., Thomma, B.P.H.J., Girardin, S.E., and Lemaitre, B. (2024). The conceptual foundations of innate immunity: Taking stock 30 years later. Immunity (Camb., Mass.) *57*, 613–631. https://doi.org/10.1016/j.immuni.2024.03.007.
3. Thaiss, C.A., Zmora, N., Levy, M., and Elinav, E. (2016). The microbiome and innate immunity. Nature *535*, 65–74. https://doi.org/10.1038/nature18847.
4. Robertson, S.J., Goethel, A., Girardin, S.E., and Philpott, D.J. (2018). Innate Immune Influences on the Gut Microbiome: Lessons from Mouse Models. Trends Immunol. *39*, 992–1004. https://doi.org/10.1016/j.it.2018.10.004.
5. Bourke, C.D., Berkley, J.A., and Prendergast, A.J. (2016). Immune Dysfunction as a Cause and Consequence of Malnutrition. Trends Immunol. *37*, 386–398. https://doi.org/10.1016/j.it.2016.04.003.
6. Lemaitre, B., Nicolas, E., Michaut, L., Reichhart, J.M., and Hoffmann, J.A. (1996). The dorsoventral regulatory gene cassette spätzle/Toll/cactus controls the potent antifungal response in Drosophila adults. Cell *86*, 973–983. https://doi.org/10.1016/s0092-8674(00)80172-5.
7. Bosco-Drayon, V., Poidevin, M., Boneca, I.G., Narbonne-Reveau, K., Royet, J., and Charroux, B. (2012). Peptidoglycan sensing by the receptor PGRP-LE in the Drosophila gut induces immune responses to infectious bacteria and tolerance to microbiota. Cell Host Microbe *12*, 153–165. https://doi.org/10.1016/j.chom.2012.06.002.

8. Capo, F., Wilson, A., and Di Cara, F. (2019). The Intestine of Drosophila melanogaster: An Emerging Versatile Model System to Study Intestinal Epithelial Homeostasis and Host-Microbial Interactions in Humans. Microorganisms *7*, 336. https://doi.org/10.3390/microorganisms7090336.

9. Hung, R.-J., Hu, Y., Kirchner, R., Liu, Y., Xu, C., Comjean, A., Tattikota, S. G., Li, F., Song, W., Ho Sui, S., and Perrimon, N. (2020). A cell atlas of the adult Drosophila midgut. Proc. Natl. Acad. Sci. USA *117*, 1514–1523. https://doi.org/10.1073/pnas.1916820117.

10. Kleino, A., and Silverman, N. (2014). The Drosophila IMD pathway in the activation of the humoral immune response. Dev. Comp. Immunol. *42*, 25–35. https://doi.org/10.1016/j.dci.2013.05.014.

11. Kaneko, T., Yano, T., Aggarwal, K., Lim, J.-H., Ueda, K., Oshima, Y., Peach, C., Erturk-Hasdemir, D., Goldman, W.E., Oh, B.-H., et al. (2006). PGRP-LC and PGRP-LE have essential yet distinct functions in the drosophila immune response to monomeric DAP-type peptidoglycan. Nat. Immunol. *7*, 715–723. https://doi.org/10.1038/ni1356.

12. Kleino, A., Ramia, N.F., Bozkurt, G., Shen, Y., Nailwal, H., Huang, J., Napetschnig, J., Gangloff, M., Chan, F.K.-M., Wu, H., et al. (2017). Peptidoglycan-Sensing Receptors Trigger the Formation of Functional Amyloids of the Adaptor Protein Imd to Initiate Drosophila NF-κB Signaling. Immunity (Camb., Mass.) *47*, 635–647.e6. https://doi.org/10.1016/j.immuni.2017.09.011.

13. Riebeling, T., Kunzendorf, U., and Krautwald, S. (2022). The role of RHIM in necroptosis. Biochem. Soc. Trans. *50*, 1197–1205. https://doi.org/10.1042/BST20220535.

14. Kleino, A., and Silverman, N. (2019). Regulation of the Drosophila Imd pathway by signaling amyloids. Insect Biochem. Mol. Biol. *108*, 16–23. https://doi.org/10.1016/j.ibmb.2019.03.003.

15. Erkosar, B., Storelli, G., Mitchell, M., Bozonnet, L., Bozonnet, N., and Leulier, F. (2015). Pathogen Virulence Impedes Mutualist-Mediated Enhancement of Host Juvenile Growth via Inhibition of Protein Digestion. Cell Host Microbe *18*, 445–455. https://doi.org/10.1016/j.chom.2015.09.001.

16. Storelli, G., Defaye, A., Erkosar, B., Hols, P., Royet, J., and Leulier, F. (2011). Lactobacillus plantarum promotes Drosophila systemic growth by modulating hormonal signals through TOR-dependent nutrient sensing. Cell Metab. *14*, 403–414. https://doi.org/10.1016/j.cmet.2011.07.012.

17. Troha, K., and Buchon, N. (2019). Methods for the study of innate immunity in Drosophila melanogaster. Wiley Interdiscip. Rev. Dev. Biol. *8*, e344. https://doi.org/10.1002/wdev.344.

18. Takehana, A., Katsuyama, T., Yano, T., Oshima, Y., Takada, H., Aigaki, T., and Kurata, S. (2002). Overexpression of a pattern-recognition receptor, peptidoglycan-recognition protein-LE, activates imd/relish-mediated antibacterial defense and the prophenoloxidase cascade in Drosophila larvae. Proc. Natl. Acad. Sci. USA *99*, 13705–13710. https://doi.org/10.1073/pnas.212301199.

19. Zhai, Z., Boquete, J.-P., and Lemaitre, B. (2018). Cell-Specific Imd-NF-κB Responses Enable Simultaneous Antibacterial Immunity and Intestinal Epithelial Cell Shedding upon Bacterial Infection. Immunity (Camb., Mass.) *48*, 897–910.e7. https://doi.org/10.1016/j.immuni.2018.04.010.

20. Rademacher, L., Lasselin, J., Karshikoff, B., Hundt, J.E., Engler, H., and Lange, T. (2021). Editorial: The Different Faces of Sickness. Front. Psychiatry *12*, 735337. https://doi.org/10.3389/fpsyt.2021.735337.

21. Okumura, T., Takeda, K., Kuchiki, M., Akaishi, M., Taniguchi, K., and Adachi-Yamada, T. (2016). GATAe regulates intestinal stem cell maintenance and differentiation in Drosophila adult midgut. Dev. Biol. *410*, 24–35. https://doi.org/10.1016/j.ydbio.2015.12.017.

22. Zhai, Z., Boquete, J.-P., and Lemaitre, B. (2017). A genetic framework controlling the differentiation of intestinal stem cells during regeneration in Drosophila. PLoS Genet. *13*, e1006854. https://doi.org/10.1371/journal.pgen.1006854.

23. Buchon, N., Osman, D., David, F.P.A., Fang, H.Y., Boquete, J.-P., Deplancke, B., and Lemaitre, B. (2013). Morphological and Molecular Characterization of Adult Midgut Compartmentalization in Drosophila. Cell Rep. *3*, 1725–1738. https://doi.org/10.1016/j.celrep.2013.04.001.

24. Hegedűs, K., Takáts, S., Boda, A., Jipa, A., Nagy, P., Varga, K., Kovács, A. L., and Juhász, G. (2016). The Ccz1-Mon1-Rab7 module and Rab5 control distinct steps of autophagy. Mol. Biol. Cell *27*, 3132–3142. https://doi.org/10.1091/mbc.E16-03-0205.

25. Li, H., You, L., Xie, J., Pan, H., and Han, W. (2017). The roles of subcellularly located EGFR in autophagy. Cell. Signal. *35*, 223–230. https://doi.org/10.1016/j.cellsig.2017.04.012.

26. Lavoie, H., Gagnon, J., and Therrien, M. (2020). ERK signalling: a master regulator of cell behaviour, life and fate. Nat. Rev. Mol. Cell Biol. *21*, 607–632. https://doi.org/10.1038/s41580-020-0255-7.

27. Houtz, P., Bonfini, A., Bing, X., and Buchon, N. (2019). Recruitment of Adult Precursor Cells Underlies Limited Repair of the Infected Larval Midgut in Drosophila. Cell Host Microbe *26*, 412–425.e5. https://doi.org/10.1016/j.chom.2019.08.006.

28. Chakrabarti, S., Liehl, P., Buchon, N., and Lemaitre, B. (2012). Infection-induced host translational blockage inhibits immune responses and epithelial renewal in the Drosophila gut. Cell Host Microbe *12*, 60–70. https://doi.org/10.1016/j.chom.2012.06.001.

29. Weinert, L.A., Araujo-Jnr, E.V., Ahmed, M.Z., and Welch, J.J. (2015). The incidence of bacterial endosymbionts in terrestrial arthropods. Proc. Biol. Sci. *282*, 20150249. https://doi.org/10.1098/rspb.2015.0249.

30. Taylor, M.J., Bordenstein, S.R., and Slatko, B. (2018). Microbe Profile: Wolbachia: a sex selector, a viral protector and a target to treat filarial nematodes. Microbiology (Read.) *164*, 1345–1347. https://doi.org/10.1099/mic.0.000724.

31. Porter, J., and Sullivan, W. (2023). The cellular lives of Wolbachia. Nat. Rev. Microbiol. *21*, 750–766. https://doi.org/10.1038/s41579-023-00918-x.

32. Pietri, J.E., DeBruhl, H., and Sullivan, W. (2016). The rich somatic life of Wolbachia. Microbiologyopen *5*, 923–936. https://doi.org/10.1002/mbo3.390.

33. Fattouh, N., Cazevieille, C., and Landmann, F. (2019). Wolbachia endosymbionts subvert the endoplasmic reticulum to acquire host membranes without triggering ER stress. PLoS Negl. Trop. Dis. *13*, e0007218. https://doi.org/10.1371/journal.pntd.0007218.

34. Toomey, M.E., Panaram, K., Fast, E.M., Beatty, C., and Frydman, H.M. (2013). Evolutionarily conserved Wolbachia-encoded factors control pattern of stem-cell niche tropism in Drosophila ovaries and favor infection. Proc. Natl. Acad. Sci. USA *110*, 10788–10793. https://doi.org/10.1073/pnas.1301524110.

35. Behrmann, L.V., Meier, K., Vollmer, J., Chiedu, C.C., Schiefer, A., Hoerauf, A., and Pfarr, K. (2024). In vitro extracellular replication of Wolbachia endobacteria. Front. Microbiol. *15*, 1405287. https://doi.org/10.3389/fmicb.2024.1405287.

36. Herren, J.K., Paredes, J.C., Schüpfer, F., Arafah, K., Bulet, P., and Lemaitre, B. (2014). Insect endosymbiont proliferation is limited by lipid availability. eLife *3*, e02964. https://doi.org/10.7554/eLife.02964.

37. Beebe, K., Robins, M.M., Hernandez, E.J., Lam, G., Horner, M.A., and Thummel, C.S. (2020). Drosophila estrogen-related receptor directs a transcriptional switch that supports adult glycolysis and lipogenesis. Genes Dev. *34*, 701–714. https://doi.org/10.1101/gad.335281.119.

38. Tennessen, J.M., Baker, K.D., Lam, G., Evans, J., and Thummel, C.S. (2011). The Drosophila estrogen-related receptor directs a metabolic switch that supports developmental growth. Cell Metab. *13*, 139–148. https://doi.org/10.1016/j.cmet.2011.01.005.

39. Michel, T., Reichhart, J.M., Hoffmann, J.A., and Royet, J. (2001). Drosophila Toll is activated by Gram-positive bacteria through a circulating peptidoglycan recognition protein. Nature *414*, 756–759. https://doi.org/10.1038/414756a.

40. Yano, T., Mita, S., Ohmori, H., Oshima, Y., Fujimoto, Y., Ueda, R., Takada, H., Goldman, W.E., Fukase, K., Silverman, N., et al. (2008). Autophagic

control of Listeria through intracellular innate immune recognition in drosophila. Nat. Immunol. *9*, 908–916. https://doi.org/10.1038/ni.1634.

41. Fukuyama, H., Verdier, Y., Guan, Y., Makino-Okamura, C., Shilova, V., Liu, X., Maksoud, E., Matsubayashi, J., Haddad, I., Spirohn, K., et al. (2013). Landscape of protein-protein interactions in Drosophila immune deficiency signaling during bacterial challenge. Proc. Natl. Acad. Sci. USA *110*, 10717–10722. https://doi.org/10.1073/pnas.1304380110.
42. Suzuki, Y.J. (2011). Cell signalling pathways for the regulation of GATA4 transcription factor: Implications for cell growth and apoptosis. Cell. Signal. *23*, 1094–1099. https://doi.org/10.1016/j.cellsig.2011.02.007.
43. Joshi, M., Viallat-Lieutaud, A., and Royet, J. (2023). Role of Rab5 early endosomes in regulating Drosophila gut antibacterial response. iScience *26*, 107335. https://doi.org/10.1016/j.isci.2023.107335.
44. Misselwitz, B., Butter, M., Verbeke, K., and Fox, M.R. (2019). Update on lactose malabsorption and intolerance: pathogenesis, diagnosis and clinical management. Gut *68*, 2080–2091. https://doi.org/10.1136/gutjnl-2019-318404.
45. Avelar Rodriguez, D., Ryan, P.M., Toro Monjaraz, E.M., Ramirez Mayans, J.A., and Quigley, E.M. (2019). Small Intestinal Bacterial Overgrowth in Children: A State-Of-The-Art Review. Front. Pediatr. *7*, 363. https://doi.org/10.3389/fped.2019.00363.
46. Sherman, P., Wesley, A., and Forstner, G. (1985). Sequential disaccharidase loss in rat intestinal blind loops: impact of malnutrition. Am. J. Physiol. *248*, G626–G632. https://doi.org/10.1152/ajpgi.1985.248.6.G626.
47. Holmes, R., and Lobley, R.W. (1989). Intestinal brush border revisited. Gut *30*, 1667–1678. https://doi.org/10.1136/gut.30.12.1667.
48. Naim, H.Y. (2001). Molecular and cellular aspects and regulation of intestinal lactase-phlorizin hydrolase. Histol. Histopathol. *16*, 553–561. https://doi.org/10.14670/HH-16.553.
49. Schwarzer, M., Gautam, U.K., Makki, K., Lambert, A., Brabec, T., Joly, A., Šrůtková, D., Poinsot, P., Novotná, T., Geoffroy, S., et al. (2023). Microbe-mediated intestinal NOD2 stimulation improves linear growth of undernourished infant mice. Science *379*, 826–833. https://doi.org/10.1126/science.ade9767.
50. Carpenter, A., and Clem, R.J. (2023). Factors Affecting Arbovirus Midgut Escape in Mosquitoes. Pathogens *12*, 220. https://doi.org/10.3390/pathogens12020220.
51. Jenkins, V.K., Larkin, A., and Thurmond, J.; FlyBase Consortium (2022). Using FlyBase: A Database of Drosophila Genes and Genetics. Methods Mol. Biol. *2540*, 1–34. https://doi.org/10.1007/978-1-0716-2541-5_1.
52. Puig, O., Marr, M.T., Ruhf, M.L., and Tjian, R. (2003). Control of cell number by Drosophila FOXO: downstream and feedback regulation of the insulin receptor pathway. Genes Dev. *17*, 2006–2020. https://doi.org/10.1101/gad.1098703.
53. Callahan, B.J., McMurdie, P.J., Rosen, M.J., Han, A.W., Johnson, A.J.A., and Holmes, S.P. (2016). DADA2: High-resolution sample inference from Illumina amplicon data. Nat. Methods *13*, 581–583. https://doi.org/10.1038/nmeth.3869.
54. McMurdie, P.J., and Holmes, S. (2015). Shiny-phyloseq: Web application for interactive microbiome analysis with provenance tracking. Bioinformatics *31*, 282–283. https://doi.org/10.1093/bioinformatics/btu616.
55. Wickham, H. (2016). ggplot2: Elegant Graphics for Data Analysis (New York: Springer-Verlag). https://doi.org/10.1007/978-3-319-24277-4.
56. Chng, W.-B.A., Sleiman, M.S.B., Schüpfer, F., and Lemaitre, B. (2014). Transforming growth factor β/activin signaling functions as a sugar-sensing feedback loop to regulate digestive enzyme expression. Cell Rep. *9*, 336–348. https://doi.org/10.1016/j.celrep.2014.08.064.
57. Mattila, J., Havula, E., Suominen, E., Teesalu, M., Surakka, I., Hynynen, R., Kilpinen, H., Väänänen, J., Hovatta, I., Käkelä, R., et al. (2015). Mondo-Mlx Mediates Organismal Sugar Sensing through the Gli-Similar Transcription Factor Sugarbabe. Cell Rep. *13*, 350–364. https://doi.org/10.1016/j.celrep.2015.08.081.
58. Zhou, Y., Zhou, B., Pache, L., Chang, M., Khodabakhshi, A.H., Tanaseichuk, O., Benner, C., and Chanda, S.K. (2019). Metascape provides a biologist-oriented resource for the analysis of systems-level datasets. Nat. Commun. *10*, 1523. https://doi.org/10.1038/s41467-019-09234-6.
59. Shannon, P., Markiel, A., Ozier, O., Baliga, N.S., Wang, J.T., Ramage, D., Amin, N., Schwikowski, B., and Ideker, T. (2003). Cytoscape: a software environment for integrated models of biomolecular interaction networks. Genome Res. *13*, 2498–2504. https://doi.org/10.1101/gr.1239303.
60. Janky, R., Verfaillie, A., Imrichová, H., Van de Sande, B., Standaert, L., Christiaens, V., Hulselmans, G., Herten, K., Naval Sanchez, M., Potier, D., et al. (2014). iRegulon: from a gene list to a gene regulatory network using large motif and track collections. PLoS Comput. Biol. *10*, e1003731. https://doi.org/10.1371/journal.pcbi.1003731.
61. Téfit, M.A., Gillet, B., Joncour, P., Hughes, S., and Leulier, F. (2018). Stable association of a Drosophila-derived microbiota with its animal partner and the nutritional environment throughout a fly population's life cycle. J. Insect Physiol. *106*, 2–12. https://doi.org/10.1016/j.jinsphys.2017.09.003.
62. Obadia, B., Keebaugh, E.S., Yamada, R., Ludington, W.B., and Ja, W.W. (2018). Diet influences host-microbiota associations in Drosophila. Proc. Natl. Acad. Sci. USA *115*, E4547–E4548. https://doi.org/10.1073/pnas.1804948115.
63. Ejsing, C.S., Sampaio, J.L., Surendranath, V., Duchoslav, E., Ekroos, K., Klemm, R.W., Simons, K., and Shevchenko, A. (2009). Global analysis of the yeast lipidome by quantitative shotgun mass spectrometry. Proc. Natl. Acad. Sci. USA *106*, 2136–2141. https://doi.org/10.1073/pnas.0811700106.

STAR★METHODS

KEY RESOURCES TABLE

REAGENT or RESOURCE	SOURCE	IDENTIFIER
Antibodies		
Anti-Armadillo	DSHB	RRID:AB_528089
Anti-Cleaved Drosophila Dcp-1 (Asp216)	Cell Signaling Technology	RRID:AB_2721060
Anti-dEGF Receptor	Merck	RRID:AB_609900
Anti-FLAG	Merck	RRID:AB_262044
Anti-Foxo (Anti-N-terminal dFoxo)	Puig et al. (2003)[52]	N/A
Anti-Mono- and polyubiquitinylated conjugates recombinant monoclonal antibody (UBCJ2)	Enzo Life Sciences	Cat# ENZ-ABS840-0100
Anti-Mouse IgG (H + L) Alexa Fluor® 647 Conjugate (red)	Cell Signaling Technology	RRID:AB_1904023
Anti-pHH3 (Anti-phospho Histone H3 (Ser 10))	Merck	RRID:AB_310177
Anti-Phospho-4E-BP1 (Thr37/46)	Cell Signaling Technology	RRID:AB_330985
Anti-Phospho-p44/42 MAPK (Erk1/2)	Cell Signaling Technology	RRID:AB_2315112
Anti-Rabbit (Cy 3-conjugated AffiniPure Donkey Anti-Rabbit IgG)	Jackson ImmunoResearch	RRID:AB_2307443
Anti-Rabbit IgG (H + L), F(ab')2 Fragment (Alexa Fluor 488 Conjugate)	Cell Signaling Technology	RRID:AB_1904025
Anti-RFP	Biozol	RRID:AB_2209751
Anti-α-Tubulin	Sigma-Aldrich	RRID:AB_477583
Chemicals, peptides, and recombinant proteins		
Active dry yeast	Bäckerei Spiegelhauer	Cat#1278
Alexa Fluor 555 Phalloidin	Cell Signaling	Cat#8953S
Ampicillin sodium salt	Sigma-Aldrich	Cat# A9518
BODIPY 493/503	Invitrogen	Cat#D3922
Erythromycin	Sigma-Aldrich	Cat# E6376
Kanamycin	Sigma-Aldrich	Cat# K1377
Methyl 4-hydroxybenzoate sodium salt	VWR	Cat#235145000
Normal donkey serum	Biozol	Cat#LIN-END9010-10
ROTI®Mount FluorCare DAPI	Carl Roth	Cat#HP20.1
Tetracycline	Sigma-Aldrich	Cat# T3258
Trametinib	Cell Signaling Technology	Cat#62206
Critical commercial assays		
β-Galactosidase Reporter Gene Staining Kit	Sigma-Aldrich	Cat# GALS-1KT
Amylase Activity Assay Kit	Sigma-Aldrich	Cat# MAK009-1KT
Amyloglucosidase from *Aspergillus niger*	Sigma-Aldrich	Cat# A1602
Bio-Rad Protein Assay Dye	Bio-Rad	Cat#5000006
DNeasy PowerSoil Pro Kit	Qiagen	Cat# 47014
Free glycerol reagent	Sigma-Aldrich	Cat#F6428-40ML
GoTaq qPCR Master Mix	Promega	Cat#A6001
Hexokinase assay Kit	Sigma-Aldrich	Cat# GAHK20
Lipase Activity Assay Kit	Sigma-Aldrich	Cat#MAK047
Pierce protease Activity Assay Kit	Thermo scientific	Cat# 23263
qScript cDNA Supermix	Quantabio	Cat#733-1178
Reliaprep RNA tissue miniprep system	Promega	Cat#Z6112
Triglyceride reagent	Sigma-Aldrich	Cat#T2449-10ML

(*Continued on next page*)

Continued

REAGENT or RESOURCE	SOURCE	IDENTIFIER
Deposited data		
mRNA-sequencing data	This paper	GEO: GSE278928
16S rRNA sequencing data	This paper	SRA: PRJNA1256711
Metabolomics data	This paper	Zenodo: 15303437
Lipidomics data	This paper	Zenodo: 15311025
Experimental Models: Organisms/Strains		
Bacteria: *Escherichia coli HTT15*	T. Hoppe	RRID:WB-STRAIN:WBStrain00041079
Bacteria: *Pseudomonas entomophila*	Leibniz Institute/DSMZ	DSM 28517
D. melanogaster: attp40: y[1] v[1]; P{y[+t7.7]=CaryP}Msp300[attP40]	BDSC	RRID:BDSC_36304
D. melanogaster: Dredd $^{-}$: y[1] w[*] Dredd[D44]	BDSC	RRID:BDSC_ 80924
D. melanogaster: UAS-ERR$_i^{BDSC_44391}$: w[*]; P{y[+t7.7] w[+mC]=UAS-ERR.RNAi}attP16/CyO	BDSC	RRID:BDSC_44391
D. melanogaster: GATAe-GFP: y[1] w[*]; P{y[+t7.7] w[+mC]=GATAe-GFP.FPTB}attP40	BDSC	RRID:BDSC_ 83656
D. melanogaster: mex-GAL4 (II): w[1118]; P{w[+mC]=mex1-GAL4.2.1}10-8	BDSC	RRID:BDSC_ 91368
D. melanogaster: mex-GAL4 (X): P{w[+mC]=mex1-GAL4.2.1}9-1, y[1] w[1118]	BDSC	RRID:BDSC_ 91367
D. melanogaster: Myo1A^{ts}: myo1A>/CyO; tub80ts/TM6B	B. Edgar	N/A
D. melanogaster: UAS-Atg1$_i^{VDRC}$: w[1118]; P{GD7149}v16133	VDRC/GD	RRID:SCR_013805, Cat#16133
D. melanogaster: UAS-Gal$_i^{TRiP}$: y[1] v[1]; P{y[+t7.7] v[+t1.8]=TRiP.HMC03081}attP2	BDSC	RRID:BDSC_ 50680
D. melanogaster: UAS-GATAe: w[1118];; UAS-GATAe	This paper	N/A
D. melanogaster: UAS-GATAe$_i^{TRiP}$: y[1] sc[*] v[1] sev[21]; P{y[+t7.7] v[+t1.8]=TRiP.HMS01087}attP2	BDSC	RRID:BDSC_ 33748
D. melanogaster: UAS-GATAe$_i^{VDRC}$: w[1118]; P{GD4152}v10418	VDRC/GD	RRID:SCR_013805, Cat#10418
D. melanogaster: mCherry-Atg8a: w; P{Atg8a_promoter-3xmCherry-Atg8a}/CyO	Hegedűs et al. (2016)[24]	N/A
D. melanogaster: UAS-PGRP-LCx: w; UAS-mCherry-PGRP-LCx/CyO; TM3,sb/TM6B	Kaneko et al. (2006)[11]	N/A
D. melanogaster: UAS-PGRP-LCx$^{\Delta 14}$: w, UAS-mCherry-PGRP-LCx[Δ14]/CyO; TM3,sb/TM6B	Kaneko et al. (2006)[11]	N/A
D. melanogaster: UAS-PGRP-LE: w[*]; P{w[+mC]=UAS-PGRP-LE.FLAG}2	BDSC	RRID:BDSC_33054
D. melanogaster: UAS-PGRP-LE$^{\Delta 14}$: w[1118];; UAS-PGRP-LE$^{\Delta 14}$	This paper	N/A
D. melanogaster: UAS-Prosα1$_i^{VDRC}$: w[1118]; P{GD17621}v49681	VDRC/GD	RRID:SCR_013805, Cat# 49681
D. melanogaster: UAS-FLAG-Rel.68: P{w[+mC]=UAS-FLAG-Rel.68}1, w[*]; TM2/TM6C, Sb[1]	BDSC	RRID:BDSC_55777
D. melanogaster infected with wmelpop IsoA3: w1118 wmelpop IsoA3	N. Kremer	N/A
Oligonucleotides		
Oligonucleotides for qPCR, see Table S4	IDT	N/A
Software and algorithms		
Cytoscape	Institute for Systems Biology (ISB) | Seattle, WA	https://cytoscape.org
Graphpad prism 8	Graphpad software	https://www.graphpad.com/scientific-software/prism/

(*Continued on next page*)

Continued

REAGENT or RESOURCE	SOURCE	IDENTIFIER
ImageJ	NIH Image	https://imagej.net/ImageJ
iRegulon	Institute for Systems Biology (ISB) | Seattle, WA	https://apps.cytoscape.org/apps/iregulon
SkanIt	Thermo Fisher Scientific	https://www.thermofisher.com
Zen	Zeiss	https://www.zeiss.com/microscopy/en/products/software/light-microscopy-software.html
R v4.3.3	R project	https://www.r-project.org
dada2 v1.34.0	Callahan et al. (2017)[53]	https://benjjneb.github.io/dada2/
phyloseq v1.50.0	McMurdie et al. (2015)[54]	https://joey711.github.io/phyloseq/
vegan v2.6.10	CRAN Repository	https://github.com/vegandevs/vegan
ggplot2 v3.5.1	Wickham (2016)[55]	https://ggplot2.tidyverse.org/index.html

EXPERIMENTAL MODEL AND STUDY PARTICIPANT DETAILS

Drosophila melanogaster strains

Unless otherwise stated, 7-to-10-day old adult males were used for experiments. Detailed lists of strains and genotypes used in these studies are provided in the key resources table and Table S5. Fly strains were routinely maintained at room temperature on a diet consisting of 0.8% agar, 8% cornmeal, 1% soymeal, 1.8% dry yeast, 8% malt extract and 2.2% sugar-beet syrup, supplemented with 0.625% propionic acid and 0.15% methyl 4-hydroxybenzoate. For experiments, adults were crossed in polypropylene bottles (Kisker Biotech, 789022B) containing a yeast-only diet (YOD, see recipe below) at room temperature. We used a yeast diet with no added sugars, as these nutrients suppress digestive activities.[56,57] For most experiments, we crossed virgin females carrying the EC-specific *mex-GAL4* driver with males carrying UAS-transgenes of interest and collected their progeny. Unless otherwise stated, progeny from the cross between *mex-GAL4* virgin females and w^{1118} males were used as controls (Table S5). Progeny were collected after adult emergence and transferred to glass vials or polystyrene vials (Kisker Biotech, 789009) at a density of 10–20 animals per vial and maintained at 25°C with a 12 h light/dark cycle. For experiments involving thermogenetic manipulations, animals were maintained at room temperature and transferred to 29°C to induce transgene expression using thermosensitive drivers. The duration of incubation at 29°C is indicated in the figure legends.

Drosophila strains were fed the following diets

YOD: 80 g active dry yeast (Bäckerei Spiegelhauer, 1278) and 10 g agar (Fisher Scientific, BP1423-2) were mixed with 1 L water and boiled on a magnetic hotplate stirrer for 10 min. After cooling to below 60°C, 4 mL of 99.5% propionic acid (Sigma-Aldrich, 81910-1L) and 5.2 g of methyl 4-hydroxybenzoate (VWR, 235145000) were added. The diet was then poured into either vials or bottles.

YOD with antibiotics: An antibiotic mixture of ampicillin (Sigma-Aldrich, A9518), kanamycin (Sigma-Aldrich, K1377), tetracycline (Sigma-Aldrich, T3258) and erythromycin (Sigma-Aldrich, E6376) was added to standard YOD prior to pouring. Antibiotics were added at a final concentration of 50 μg/mL (ampicillin, kanamycin and tetracycline) or 15 μg/mL (erythromycin). This diet has been used to cure *Wolbachia* infection and to maintain germ-free stocks (see sections "Infection with *Wolbachia*" and "Generation of germ-free stocks" below).

YOD with trametinib: trametinib (Cell signaling technology, 62206S) was dissolved in dimethylsulfoxide (DMSO) and added to a final concentration of 30 μM in YOD prior to pouring. Diets supplemented with DMSO alone were used as controls.

YOD without preservatives: 80 g active dry yeast (Bäckerei Spiegelhauer, 1278) and 10 g agar (Fisher Scientific, BP1423-2) were mixed with 1 L water in a glass bottle with screw cap and autoclaved. The diet was then poured into autoclaved glass vials and immediately used for experiments. This diet was used for experiments involving microbiome profiling, *16S rRNA* qPCR analysis, and quantification of lactic acid bacteria in midgut homogenates.

YOD without preservatives but with tetracycline: same recipe as above, but the diet was supplemented with tetracycline at a final concentration of 10 μg/mL. This diet was used to monoassociate germ-free flies with *E. coli HT115* (see section "Monoassociation with *E. coli*" below).

Generation of germ-free stocks

Germ-free stocks were established by collecting embryos, placing them in a mesh sieve and bathing them in 50% bleach (v/v) for 5 min for dechorionation. Embryos were then bathed in 70% ethanol (v/v) for 3 min, followed by 2 min in sterile water. Dechorionated, sterile embryos were then transferred to autoclaved polypropylene bottles containing YOD with antibiotics (recipe described above). Germ-free status was checked weekly by plating fly homogenates on LB and MRS agar.

Bacterial strains

Pseudomonas entomophila and *E. coli HT115* were routinely cultured in lysogeny broth. For *E. coli HT115*, lysogeny broth was supplemented with 10 μg/mL of tetracycline (Sigma-Aldrich# T3258), because this strain carries a tetracycline resistance cassette in its chromosome. Bacterial cultures were performed and prepared for inoculations as described below. *Wolbachia* are obligate endosymbionts, and cannot be cultured outside of their hosts. *Drosophila* stocks naturally infected with these endosymbionts were used for vertical transmission, as described below.

Infection with *Pseudomonas entomophila*

Pseudomonas entomophila was cultured in lysogeny broth at 30°C and 180 rpm for 12 h. The bacterial culture was then centrifuged at 3.000 rpm for 10 min at 4°C. After discarding the supernatant, the bacterial pellet was resuspended in PBS to reach an optical density (600 nm) of 100. 150 μL of this bacterial solution was inoculated on the surface of food that was previously lacerated with a pipet tip. Food was inoculated with PBS for negative controls. 10 to 15 flies were transferred to vials inoculated with PBS or *Pseudomonas entomophila* after 16 h of wet starvation. For wet starvation, adults were transferred to vials containing a dense weave cellulose acetate stopper (Kisker# 789035) saturated with tap water. The vials were sealed with a second (dry) cellulose acetate stopper to limit water loss by evaporation. Wet starvation was performed at 25°C and was used to increase the motivation to ingest contaminated food after flies are transferred to vials inoculated with *Pseudomonas entomophila*. Animals were incubated with *Pseudomonas entomophila* for 48 h before being collected for experiments.

Monoassociation with *E. coli*

Newly-eclosed germ-free adults were transferred to food inoculated with 150 μL of PBS or with 150 μL of *E. coli HT115* suspended in PBS. The bacterial inoculum was prepared as described above, except that *E. coli* was initially cultured in lysogeny broth supplemented with 10 μg/mL of tetracycline (Sigma-Aldrich# T3258) at 37°C and 180 rpm for 12 h. Bacteria were then pelleted by centrifugation and resuspended in PBS to reach an optical density (600 nm) of 10. YOD without preservatives was used for these experiments to avoid any possible negative effect on *E. coli* survival. However, food was supplemented with tetracycline at 10 μg/mL to avoid contamination with environmental bacteria. Vials were laid horizontally to prevent flies from sticking to the food. Flies were allowed to mature for seven days under these conditions, after which they were collected for experiments.

Infection with *Wolbachia* and endosymbiont removal

For experiments involving *Wolbachia* quantification in a *Dredd* mutant background, we used the $Dredd^{D44}$ line (RRID:BDSC_80924) to transmit infection, as we found that it naturally carries this endosymbiont. $Dredd^{D44}$ females were used to generate (via crosses) a *Wolbachia*-positive line carrying the $Dredd^{D44}$ mutation and the *mex-GAL4* driver. *Wolbachia*-positive, $Dredd^{D44}$*; mex-GAL4* females were then crossed with w^{1118} males or males carrying a *UAS-PGRP-LE* transgene for experiments.

For all other experiments, we used a w^{1118} stock infected with the *Wolbachia* strain wMelPop (IsoA3) (stock provided by Natacha Kremer, Université de Lyon, France). Females from this stock were used to generate (via crosses) a *Wolbachia*-positive line carrying the *mex-GAL4* driver. *Wolbachia*-positive, *mex-GAL4* females were then crossed with w^{1118} males or males carrying the different *UAS-RNAi* transgenes for experiments.

The $Dredd^{D44}$ line was cleared of *Wolbachia* by rearing animals on a diet containing antibiotics (see the section "*Drosophila* strains and handling") for four generations. *Wolbachia* elimination was verified by PCR and *16S rRNA* sequencing on genomic DNA extracted from whole flies and guts, respectively. These animals were then maintained on diets containing antibiotics for several additional generations to keep them germ-free before being used for metabolomics analysis (Figure 3E). Alternatively, *Wolbachia*-free $Dredd^{D44}$ mutants were transferred back to antibiotic-free diets for several generations to re-acquire natural commensals and be used for microbiome sequencing (Figure 6).

METHOD DETAILS

Generation of the *UAS-PGRP-LE*$^{\Delta 14}$ transgenic line

The *PGRP-LE* coding sequence with a deletion in the cRHIM domain ($PGRP\text{-}LE^{\Delta 14}$) was synthesized by Integrated DNA Technologies and cloned into the pIDTSMART-AMP+ vector. After digestion with KpnI-HF and NotI-HF (NEB R3142S and R3189S, respectively), the $PGRP\text{-}LE^{\Delta 14}$ coding sequence was ligated into the pUAST-attB vector (RRID:DGRC_1419) using T4 ligase (NEB M0202S). The resulting plasmid was transformed into *E. coli DH5α* for amplification and was isolated using the QIAfilter plasmid midi kit (Qiagen# 12243). The plasmid was injected into *y[1] M{p3xP3-EGFP.vas-int.Dm}ZH-2A M{3xP3-RFP.attP} w*;; P{CaryP}attP2* embryos for genomic insertion. Transgenic flies were backcrossed to the w^{1118} background.

Generation of the *UAS-GATAe* transgenic line

The full-length *GATAe* open reading frame was obtained from clone LD08432 from the *Drosophila* Genomic Resource Center (RRID:DGRC_5060; https://dgrc.bio.indiana.edu//stock/5060). Briefly, the *GATAe* open reading frame was obtained after plasmid digestion with KpnI-HF and NotI-HF (NEB R3142S and R3189S, respectively) and ligated into the pUAST-attB vector (RRID:DGRC_1419) using T4 ligase (NEB, M0202S). Subsequent steps to generate the *UAS-GATAe* transgenic line were performed as described above.

RNA extraction and cDNA synthesis

Five flies or ten midguts were collected in homogenization microtubes containing 100 μL of sterile glass beads (1 mm diameter) and snap frozen in liquid nitrogen. Samples were stored at −80°C until RNA extraction. Total RNA was extracted using the Reliaprep RNA Tissue Miniprep System (Promega, Z6112). 500 μL of lysis buffer was added to the microtubes and tissues were homogenized using a Precellys 24 (Bertin technologies) at 5,000 rpm for 15 s. Subsequent steps for RNA extraction were performed according to the manufacturer's recommendations. Reverse transcription was performed on 0.25–1 μg RNA using qScript cDNA Supermix (Quantabio, 733–1178) following the manufacturer's recommendations. cDNA was used for qPCR analyses as described below.

mRNA sequencing

20 intestines were dissected in PBS on ice and snap frozen in liquid nitrogen. Five biological replicates per genotype were generated and total RNA was extracted as described above. Library preparation and sequencing were performed by the Cologne Center for Genomics. Libraries were prepared using the Illumina Stranded Truseq RNA Sample Preparation Kit. ERCC RNA Spike-In Mix (ThermoFisher Scientific, 4456740) was added to the samples prior to library preparation. 1 μg of total RNA was used for library preparation. After poly-A selection (using poly-T oligo-attached magnetic beads), mRNA was purified and fragmented using divalent cations at elevated temperature. RNA fragments were reverse transcribed using random primers and second-strand cDNA synthesis was performed with DNA polymerase I and RNase H. After end repair and A-tailing, indexing adapters were ligated. The products were purified and amplified (15 PCR cycles) to generate the final cDNA libraries. After library validation and quantification (Agilent Tape Station), equimolar amounts were pooled. The pool was quantified by using the Peqlab KAPA Library Quantification Kit and the Applied Biosystems 7900HT Sequence Detection System. The pool was sequenced on an Illumina NovaSeq6000 sequencing instrument using a PE100 protocol.

Transcriptomic and GO term analysis

The quality of the sequencing reads was checked using FastQC. Sequencing reads were trimmed by using Trim Galore! software (https://www.bioinformatics.babraham.ac.uk/projects/trim_galore/) and the following adapters:

Read1.

(1) AGATCGGAAGAGCACACGTCTGAACTCCAGTCA
(2) AGATCGGAAGAGCACACGTCTGAAC
(3) TGGAATTCTCGGGTGCCAAGG
(4) AGATCGGAAGAGCACACGTCT
(5) CTGTCTCTTATACACATCT
(6) AGATGTGTATAAGAGACAG

Read2.

(1) AGATCGGAAGAGCGTCGTGTAGGGAAAGAGTGT
(2) AGATCGGAAGAGCGTCGTGTAGGGA
(3) TGGAATTCTCGGGTGCCAAGG
(4) AGATCGGAAGAGCACACGTCT
(5) CTGTCTCTTATACACATCT
(6) AGATGTGTATAAGAGACAG

D. melanogaster annotated transcripts (BDGP6.32) were downloaded from Ensembl. Transcript abundance was estimated by using Kallisto-quant (https://pachterlab.github.io/kallisto/manual, ver. 0.46.2.). Read count normalization was performed by adjusting to ERCC spike-in controls and differential gene expression analysis was performed by RUVSeq and edgeR Bioconductor R packages. Gene ontology term enrichment analysis was performed with Metascape.[58]

TF binding site analysis

We used Cytoscape[59] with the iRegulon plugin[60] to analyze the enrichment of putative TF binding sites in the vicinity of genes whose transcripts are significantly downregulated in *Dredd* mutant intestines with *PGRP-LE* overexpression in enterocytes. Table S3 lists the parameters used for the analysis and shows for each motif the matching candidate TFs and the target genes containing this motif in their vicinity (5kb upstream and full transcript).

DNA extraction

5 flies, 15 midguts or 10 pairs of ovaries were collected in homogenization microtubes containing 100 μL of sterile glass beads (1 mm diameter) and snap frozen in liquid nitrogen. Samples were stored at −80°C until DNA extraction. The DNeasy PowerSoil Pro Kit (Qiagen, 47014) was used for genomic DNA extraction. 800 μL of CD1 solution was added to the microtubes and tissues were homogenized using a Precellys 24 (Bertin technologies) at 5,000 rpm for 15 s. Homogenates were then transferred to PowerBead Pro tubes. The PowerBead Pro tubes were attached to a vortex adapter (Carl Roth, P510.1 and P509.1) and vortexed at high speed for 10 min.

After centrifugation at 15,000 x g for 1 min, the supernatants were transferred to a clean 2 mL microcentrifuge tube. Subsequent steps for DNA extraction were performed according to the manufacturer's recommendations. Genomic DNA was eluted in 50 μL of Solution C6 and used for microbiome profiling and qPCR analyses as described below.

Microbiome profiling

Drosophila were reared on a diet containing preservatives until adult eclosion, after which they were transferred to a preservative-free diet (see composition in "*Drosophila* strains and handling"). Preservatives were omitted because they have microbiocidal properties and limit the density and diversity of gut bacteria.[61,62] Animals were fed these diets for five days in vials laid horizontally to prevent insects from sticking to the food. Animals were then anesthetized and washed once in 70% ethanol for 3 s and twice in sterile PBS for 3 s each. Intestines were dissected for DNA extraction, as described above. Subsequent sequencing was performed by Eurofins Genomics. Sequencing libraries were generated after amplification of the V3-V4 hypervariable regions of the bacterial *16S rRNA* gene in genomic DNA. The libraries were subjected to Illumina MiSeq 300 bp paired-end sequencing. Sequencing data were processed in R (v.4.4.3) using the Divisive Amplicon Denoising Algorithm 2 pipeline ("dada2" package v.1.34.0) with recommended parameters (https://benjjneb.github.io/dada2/tutorial.html).[53] The Silva taxonomic database (v.138.2) was used for taxonomic assignment of amplicon sequence variants (ASVs). Unassigned ASVs were excluded from further analysis. Diversity analysis was performed using the "phyloseq" package (v.1.50.0).[54] Alpha diversity for within-sample richness and evenness was carried out using the Shannon-Wiener and Simpson indices. Beta diversity was assessed by permutational multivariate analysis of variance ("PERMANOVA, "adonis2" function, "vegan" package v.2.6.10) based on unweighted UniFrac distances and principal coordinate analysis visualization. ggplot2 was used for graphical representation of the data.[55]

Quantitative PCR (qPCR)

Genomic or cDNA was used as template with GoTaq qPCR Master Mix (Promega, A6001). qPCR reactions were performed according to the manufacturer's recommendations on a Quantstudio 3 instrument (Applied Biosystem). Fold change in genomic sequences or in transcript levels were determined using the ΔΔCt method. For RT-qPCR analyses, transcript levels were normalized to *rp49* (also known as *RpL32*). Oligonucleotides specific for *Lactiplantibacillus 16S rRNA* (*16S rRNA Lp*) or allowing universal *16S rRNA* amplification (*16S rRNA Uni*) were used to score *Lactiplantibacillus* and total bacterial load, respectively, in genomic DNA extracted from whole flies. The level of *16S rRNA* genomic sequence was normalized to *Drosophila Act5C* genomic sequence ("$_g$*Act5C*"). For *Wolbachia* quantification, oligonucleotides were designed to amplify a portion of *Wolbachia dnaA* based on the complete genome sequence of *Wolbachia* sp. wRi (GenBank: CP001391.1). The level of *dnaA* genomic sequence was normalized to *Drosophila Act5C* genomic sequence ("$_g$*Act5C*"). qPCR analyses were performed in three to five biological replicates. Independent experiments were repeated two to three times. A list of oligonucleotides used for qPCR analyses is provided in Table S4. All qPCR data are presented in Table S6, together with the *p*-values obtained from statistical tests.

Quantification of lactic acid bacteria by plating

Drosophila were reared on a diet containing preservatives until adult eclosion, after which they were transferred to a preservative-free diet (see composition in "*Drosophila* melanogaster strains"). Animals were maintained at 25°C for five days in vials laid horizontally to prevent insects from sticking to the food. Animals were then anesthetized and washed once in 70% ethanol for 3 s and twice in sterile PBS for 3 s each. Midguts were then dissected in sterile PBS and individual organs were homogenized in microtubes containing 100 μL of sterile 1 mm glass beads and 500 μL of sterile PBS using a Precellys 24 (Bertin technologies) at 5,000 rpm for 15 s. Dilutions of intestinal homogenates were then plated onto De Man Rogosa Sharpe (MRS) agar media (Carl Roth, X924.1) using an automated spiral plater (Interscience easySpiral Pro, ref# 413 000). The agar plates were then incubated at room temperature for four days and the number of colony-forming units was determined using an automated colony counter (Interscience Scan 300, ref# 436 300).

Measurement of digestive activities

Intestinal amylase, protease and lipase activities were quantified in biological replicates containing 5, 10 and 30 midguts, respectively. Midguts were dissected in PBS on ice, collected in homogenization microtubes containing 100 μL of sterile glass beads (1 mm diameter) and snap frozen in liquid nitrogen. Samples were stored at −80°C until assayed for enzymatic activity. Amylase assay kit (Sigma-Aldrich, MAK009), Pierce colorimetric protease assay kit (Thermo Scientific, 23263) and lipase activity assay kit (Sigma-Aldrich, MAK047) were used with a Multiscan SkyHigh microplate spectrophotometer (Thermo Fisher scientific) to measure the respective enzymatic activities. 90, 130 or 90 μL of assay buffer from the amylase, protease and lipase kits, respectively, were added to frozen midgut samples. Midguts were then rapidly homogenized using a Precellys 24 (Bertin technologies) at 5,000 rpm for 15 s and homogenates were centrifuged at 13,000 x g for 10 min at 4°C to precipitate insoluble material. 50 μL of supernatant was transferred to a 96-well plate and subsequent steps were performed according to the manufacturer's recommendations. Intestinal amylase, protease and lipase activities were normalized to the number of midguts in samples.

Immunostaining and signal quantification

Tissues were dissected in PBS, fixed in 4% paraformaldehyde for 1 h at room temperature, and rinsed three times in PBS 0.5% Triton X-100 (PBST). Samples were then incubated in blocking buffer (5% normal donkey serum (Biozol, LIN-END9010-10) in PBST) for 12 h

at 4°C. Samples were then incubated in primary antibody diluted in blocking buffer for at least 12 h at 4°C. Tissues were then rinsed twice and washed for 1 h in PBST. They were incubated in secondary antibody (diluted in blocking buffer) for 2 to 3 h in the dark and at room temperature. Following dilutions were used: anti-Armadillo: 1:20, anti-dEGFR: 1:200, anti-cleaved Dcp-1, Foxo,[52] p-4E-BP: 1:200, anti-FLAG: 1:300, anti-mono/polyubiquitinylated conjugates: 1:250, anti-pHH3, RFP: 1:500, anti *p*-ERK: 1:100. All secondary antibodies were diluted 1:500 before use. Tissues were then rinsed twice in PBST and washed in PBS for 1 h before mounting in RotiMount FluorCare DAPI mounting medium (Carl Roth, HP20.1). Tissues were imaged using a BX53 fluorescence microscope (Olympus) or an LSM 710 confocal microscope (Zeiss). Two to three independent stains were performed on sets of 5–15 tissues. A representative image is shown in the figures. For quantification of pHH3- and cleaved Dcp-1-positive cells, cells were manually counted in the whole midgut or in the anterior midgut (R1 and R2), respectively. To measure nuclear Foxo fluorescence, TIFF images of the DAPI channel were opened with ImageJ and a threshold was manually applied to selectively outline nuclei. A mask was created and a watershed was applied to individualize nuclei. Relevant nuclei were further filtered based on size using the "analyze particles" command. This "nuclear ROI" was then applied to the TIFF image of the anti-Foxo stain to measure the mean pixel gray value. Mono/polyubiquitinylated particles were quantified in frontal views of R2 obtained by confocal microscopy. Images of the corresponding channel were opened with ImageJ and a threshold was manually applied to detect stained particles. Particles were then quantified using the "analyze particles" command. Only particles with a size between 18-infinity pixels were considered for analysis. EGFR was quantified in transverse views of R2 obtained by confocal microscopy. Images were opened with ImageJ and the area of the epithelial monolayer was quantified using the polygon selection tool. The area outside the epithelial monolayer was cleared using the "clear outside" command, and channels were split into different images. The channel for the anti-EGFR antibody stain was selected and a threshold was manually applied to measure EGFR-positive particles. The cumulative area of EGFR-positive particles was then divided by the area of the epithelial monolayer for normalization. p-4E-BP and p-ERK fluorescence signal was quantified in whole midgut images taken with a wide field fluorescence microscope. Images were opened with ImageJ and converted to 8-bit. Midguts were manually outlined using the polygon selection tool and the mean pixel gray value was measured on these selections. We subtracted the minimum pixel gray value in the selection from the mean pixel gray value to subtract background fluorescence.

Bodipy and phalloidin stains

After fixation and immunostaining (see details above), tissues were incubated in the dark in 2 μg/mL BODIPY 493/503 (Invitrogen, D3922) and 33 nM Alexa Fluor 555 Phalloidin (Cell Signaling Technology, 8953S) in PBS for 1 h. After incubation, tissues were washed three times in PBS and mounted in RotiMount FluorCare DAPI mounting medium (Carl Roth, HP20.1). Images were captured with a BX53 fluorescence microscope (Olympus) or an LSM 710 confocal microscope (Zeiss).

Quantification of fluorescent reporter signal

Tissues expressing GFP-tagged GATAe (*GATAe-GFP*) were rapidly dissected in PBS, fixed in 4% paraformaldehyde for 30 min at room temperature, rinsed three times in PBS, and mounted in RotiMount FluorCare DAPI mounting medium (Carl Roth, HP20.1). Tissues were imaged immediately after mounting. Nuclear GATAe-GFP signal was quantified as described above for Foxo immunostaining. Tissues expressing mCherry-tagged Atg8a (*mCherry-Atg8a*) were dissected in PBS, fixed in 4% paraformaldehyde and immunostained with anti-RFP antibodies, as described above. The number of mCherry-positive particles in intestines expressing *mCherry-Atg8a* was determined using the "analyze particles" command in ImageJ.

X-gal stains

X-gal stains were performed using the β-galactosidase reporter gene staining kit (Sigma-Aldrich, GALS-1KT). Steps were performed according to the manufacturer's protocol. Briefly, tissues were dissected in PBS and incubated in fixation solution for 10 min at room temperature. Tissues were then washed twice in PBS and incubated in the staining solution for 1 to 2 h at 37°C. Tissues were then washed twice in PBS before mounting in glycerol. Tissues were imaged using a BX53 widefield microscope (Olympus). Two to three independent stains were performed on sets of 10–15 tissues. A representative image is shown in the figures.

Metabolite assays

Whole-body glycogen and glucose levels were determined using the hexokinase assay kit (Sigma-Aldrich, GAHK20) and amyloglucosidase (Sigma-Aldrich, A1602-25MG). Whole-body triglyceride levels were determined using the triglyceride reagent (Sigma-Aldrich, T2449-10ML) and the free glycerol reagent (Sigma-Aldrich, F6428-40ML). Whole-body protein levels were determined using the protein assay dye (Bio-Rad, 5000006).

Metabolite assays were performed as follows: five decapitated flies were homogenized using a motor and pestle in either 120 μL ice-cold PBS (for the determination of glucose and glycogen) or 120 μL of ice-cold PBS containing 0.05% Tween 20 (for the determination of triglycerides). Immediately after homogenization, 10 μL of homogenates were diluted in 90 μL PBS for protein quantification. 10 μL of this solution was mixed with 200 μL of Bio-Rad Protein Assay Dye (Cat#5000006, diluted 1:4 in Milli-Q water (v/v)) and incubated for 5 min at room temperature. Absorbance was then read at 595 nm using a Multiscan SkyHigh microplate spectrophotometer (Thermo Fisher scientific). The protein concentration in homogenates was determined using a standard curve generated with diluted BSA samples that had been treated with Bio-Rad Protein Assay Dye.

After homogenization and taking 10 μL for protein quantification, the remaining fly homogenates were immediately incubated at 70°C for 10 min in a water bath to inactivate endogenous enzymes.

To determine triglyceride concentration, 30 μL of heat-treated homogenates was incubated with either 30 μL of PBS ("untreated samples") or 30 μL of triglyceride reagent for 1 h at 37°C, after which they were centrifuged at maximum speed for 3 min at 4°C. Then, 30 μL of the supernatant was transferred to a 96-well plate and incubated with 100 μL of free glycerol reagent for 5 min at 37°C to determine the free glycerol concentration. Absorbance was then read at 540 nm using a Multiscan SkyHigh microplate spectrophotometer (Thermo Fisher scientific). The absorbance of untreated samples was then subtracted from that of samples incubated with triglyceride reagent. This value was then used to calculate the triglyceride content of each sample based on a standard curve of serial dilutions of a triolein-equivalent (triolein equivalent glycerol standard 2.5 mg/mL, Sigma-Aldrich, G7793) treated with the free glycerol reagent.

To measure whole body glycogen and glucose levels, heat-treated fly homogenates were centrifuged at maximum speed for 3 min at 4°C, and 10 μL of the supernatant was diluted in 40 μL PBS. 15 μL was transferred to a 96-well plate and incubated with either 15 μL of PBS ("untreated" samples), or 15 μL of amyloglucosidase diluted in PBS (1.5 μL of amyloglucosidase stock solution diluted in 1 mL PBS) for 1 h at 37°C. Samples were then incubated with 100 μL of hexokinase reagent for 2 h at room temperature. Absorbance was then read at 340 nm using a Multiscan SkyHigh microplate spectrophotometer (Thermo Fisher scientific). To determine glycogen levels, the absorbance measured for free glucose in the untreated samples was subtracted from that of the absorbance of the samples digested with amyloglucosidase. The glycogen content of each sample was then calculated based on a standard curve with serial dilutions of glycogen (Sigma-Aldrich, G0885) digested with amyloglucosidase and treated with the hexokinase reagent as described above. To determine the free glucose level, the absorbance measured for free glucose in the untreated samples was calculated based on a standard curve with serial dilutions of glucose treated with the hexokinase reagent. Triglyceride, glucose and glycogen were normalized to protein contents.

Samples extraction of polar metabolites

For metabolite extraction, 40 midguts were collected in 2 mL Eppendorf tubes containing a 5 mm metal ball. These tubes were stored in liquid nitrogen before being ground to a fine powder using a TissueLyser (Qiagen) set at 25 Hz for 1 min. Immediately after homogenization, 1 mL of a −20°C acetonitrile:methanol:water (4:4:2 (v/v:v)) mixture, containing 250 nM U-13C15N amino acid mix (Cambridge isotopes, MSK_A2-1.2), each 0.1 μg/mL stock solution of 13C10 ATP, 15N5 ADP and 13C1015N5 AMP (Sigma) and 0.05 μg/mL deuterated citric acid (citric acid D4, Sigma), were added. The extraction solvents were all (UPLC-grad, Biosolve). After the addition of the extraction buffer, the samples were immediately vortexed for 10 s and incubated on an orbital shaker at 4°C for another 30 min. To remove the insoluble material, the metal balls were removed from each sample using a magnet and the tubes were centrifuged at 21,000× g for 10 min at 4°C. The cleared supernatant was transferred to fresh 1.5 mL Eppendorf tubes and immediately concentrated to complete dryness in a speed vacuum concentrator at room temperature (ScanVac, Labogene). Dried samples were processed immediately for LC-MS analysis.

Metabolomics (anionic metabolites)

Anionic metabolites were analyzed by anion-exchange chromatography mass spectrometry (AEX-MS). Extracted metabolites were resuspended in 150 μL of UPLC/MS grade water (Biosolve). Samples were immediately vortexed for 10 s and then incubated for 15 min at 4°C on an orbital shaker. To remove insoluble material, the tubes were centrifuged at 15,000 x g for 5 min at 4°C. The cleared supernatant was transferred to a fresh 1.5 mL Eppendorf tube, from which 100 μL was transferred to polypropylene autosampler vials (Chromatography Accessories Trott, Germany).

Samples were analyzed using a Dionex ion chromatography system (Integrion Thermo Fisher Scientific). 5 μL of polar metabolite extract was injected in push partial mode, using an overfill factor of 1, onto a Dionex IonPac AS11-HC column (2 mm × 250 mm, 4 μm particle size, Thermo Fisher Scientific) equipped with a Dionex IonPac AG11-HC guard column (2 mm × 50 mm, 4 μm, Thermo Fisher Scientific). The column temperature was held at 30°C, while the autosampler was set at 6°C. A potassium hydroxide gradient was generated using a potassium hydroxide cartridge (Eluent Generator, Thermo Scientific), which was supplied with deionized water (Millipore). Metabolite separation was performed at a flow rate of 380 μL/min, applying the following gradient conditions: 0–3 min, 10 mM KOH; 3–12 min, 10−50 mM KOH; 12–19 min, 50–100 mM KOH; 19–22 min, 100 mM KOH, 22–23 min, 100-10 mM KOH. The column was re-equilibrated at 10 mM for 3 min.

For the analysis of metabolic pool sizes, the eluting compounds were detected in negative ion mode using full scan measurements in the mass range m/z 77–770 on a Q-Exactive HF high-resolution MS (Thermo Fisher Scientific). The heated electrospray ionization (HESI) source settings of the mass spectrometer were: Spray voltage 3.2 kV, capillary temperature was set to 300°C, sheath gas flow 50 AU, aux gas flow 20 AU at a temperature of 330°C and a sweep gas glow of 2 AU. The S-lens was set to a value of 60.

Semi-targeted LC-MS data analysis was performed using TraceFinder software (Version 5.1, Thermo Fisher Scientific). The identity of each compound was validated by authentic reference compounds, which were measured at the beginning and the end of the sequence. For data analysis, the area of the deprotonated $[M\text{-}H^{+}]^{-1}$ or doubly deprotonated $[M\text{-}2H]^{-2}$ monoisotopologue mass peaks of each required compound was extracted and integrated with a mass accuracy of <3 ppm and a retention time (RT) tolerance of <0.05 min compared to the independently measured reference compounds. These areas were then normalized to the internal standards added to the extraction buffer, followed by a normalization to the total protein content of the analyzed sample.

Metabolomics (amine-containing metabolites)

Amine-containing metabolites were analyzed by semi-targeted liquid chromatography-high-resolution mass spectrometry-based (LC-HRS-MS). 50 μL of the available 150 μL of the above mentioned (AEX-MS) polar phase were mixed with 25 μL of 100 mM sodium carbonate (Sigma), followed by the addition of 25 μL 2% [v/v] benzoylchloride (Sigma) in acetonitrile (UPC/MS-grade, Biosove). Derivatized samples were thoroughly mixed and stored at 20°C until analysis.

For the LC-HRMS analysis, 2 μL of the derivatized sample was injected onto a 100 × 2.1 mm HSS T3 UPLC column (Waters). The flow rate was set at 400 μL/min using a binary buffer system consisting of buffer A (10 mM ammonium formate (Sigma), 0.15% [v/v] formic acid (Sigma) in UPC-MS-grade water (Biosove, Valkenswaard, Netherlands). Buffer B consisted of acetonitrile with 0.1% [v/v] formic acid (UPLC-MS grade, Biosove). The column temperature was set at 40°C, while the LC gradient was: 0% B at 0 min, 0–15% B 0- 4.1min; 15–17% B 4.1–4.5 min; 17–55% B 4.5–11 min; 55–70% B 11–11.5 min, 70–100% B 11.5–13 min; B 100% 13–14 min; 100-0% B 14–14.1 min; 0% B 14.1–19 min; 0% B. The mass spectrometer (Q-Exactive Plus, Thermo Fisher Scientific) was operating in positive ionization mode recording the mass range m/z 100–1000. The heated ESI source settings of the mass spectrometer were: Spray voltage 3.5 kV, capillary temperature 300°C, sheath gas flow 60 AU, aux gas flow 20 AU at 330°C, and the sweep gas was set to 2 AU. The RF-lens was set to a value of 60. Semi-targeted data analysis of the samples was performed using TraceFinder software (version 5.1, Thermo Fisher Scientific). The identity of each compound was validated by authentic reference compounds, which were run before and after each sequence. Peak areas of $[M + nBz + H]^+$ ions were extracted with a mass accuracy (<3 ppm) and a retention time tolerance of <0.05 min. Areas were calculated as described in the AEX-MS method.

Fatty acid profiling

For each genotype, five samples of ten male flies were collected and stored at −80°C until determination of fatty acid (FA) levels. Samples were rapidly homogenized in 300 μL Milli-Q water using a Precellys 24 device (Bertin technologies) at 6500 rpm for 30 s. The protein content of the homogenate was determined using bicinchoninic acid. 500 μL of methanol, 250 μL of chloroform and internal standard (0.5 μg palmitic-d31 acid) were added to fly homogenates (100 μL). The mixture was sonicated for 5 min, and lipids were extracted in a shaking bath at 48°C overnight. Glycerolipids were degraded by alkaline hydrolysis by adding 75 μL of 1 M potassium hydroxide in methanol. After sonication for 5 min, the extract was incubated for 2 h at 37°C and neutralized with 6 μL of glacial acetic acid. 2 mL of chloroform and 4 mL of water were added to the extract, which was vortexed vigorously for 30 s and centrifuged (4,000 x g, 5 min, 4°C) to separate the layers. The lower (organic) phase was transferred to a new tube, and the upper phase was extracted with 2 mL of chloroform. The combined organic phases were dried under a nitrogen stream. Residues were resolved in 200 μL of acetonitrile/water (2:1, volume/volume) and sonicated for 5 min. After centrifugation (12,000 x g, 10 min, 4°C), 40 μL of the supernatants were transferred to autoinjector vials. FA content was determined by LC-ESI-MS/MS. 10 μL of sample was loaded onto a Core-Shell Kinetex Biphenyl column (100 mm × 3.0 mm ID, 2.6 μm particle size, 100Å pore size, Phenomenex), and fatty acids were detected using a QTRAP 6500 triple quadrupole/linear ion trap mass spectrometer (SCIEX). The LC (Nexera X2 UHPLC System, Shimadzu) was operated at 40°C and at a flow rate of 0.7 mL/min with a mobile phase of 5 mM ammonium acetate and 0.012% acetic acid in water (solvent A) and acetonitrile/isopropanol 80:20 (v/v) (solvent B). Fatty acids were eluted with the following gradient: initial, 55% B; 4 min, 95% B; 7 min, 95% B; 7.1 min, 55% B; 10 min, 55% B.Fatty acids were monitored in negative ion mode using "pseudo" Multiple Reaction Monitoring (MRM) transitions.[63] The instrument settings for nebulizer gas (Gas 1), turbogas (Gas 2), curtain gas, and collision gas were 60 psi, 90 psi, 40 psi, and medium, respectively. The interface heater was on, the Turbo V ESI source temperature was 650°C, and the ionspray voltage was −4 kV. The LC chromatogram peaks of the endogenous fatty acids and the internal standard palmitic-d31 acid were integrated using the MultiQuant 3.0.2 software (SCIEX). Endogenous fatty acids were quantified by normalizing their peak areas to those of the internal standard. The normalized peak areas were then normalized to the protein content of the homogenate.

Western blot

20 guts were lysed in protein lysis buffer (50 mM Tris-HCl at pH 7.8, 150 mM NaCl, 0.25% sodium deoxycholate, 1 mM EDTA and protease inhibitor cocktail (Sigma-Aldrich, 11836153001)) using a Precellys 24 device (Bertin technologies). Tissues were homogenized twice at 5.500 rpm for 30 s with a 15 s pause. Homogenates were centrifuged at 10.000 x g for 10 min at 4°C to precipitate insoluble material. Protein concentrations in supernatant was determined with Pierce BCA protein assay (ThermoScientific, 23225). 15 μg of protein was separated by SDS–polyacrylamide gel electrophoresis, transferred to nitrocellulose membranes and subjected to immunoblotting. Western blot analysis was performed with anti-mono/polyubiquitinylated conjugates (diluted 1:1000) and anti-α-Tubulin (diluted 1:5000).

Quantification of locomotor activity

Locomotor activity was recorded using DAM2 *Drosophila* activity monitors and DAMSystem3 data collection software (TriKinetics Inc). Individual flies were rapidly anesthetized and placed in 5 mm Pyrex glass tubes (TriKinetics Inc USA) with a food supply. The ends of the glass tubes were sealed with parafilm (Heathrow Scientific) and the tubes were placed in activity monitors. Monitors were placed in a 25°C incubator with a 12-h light/dark cycle. Animals were acclimated for two full days before locomotor activity was recorded for three days. Animals that died before the end of the recording period were censored from the analysis.

QUANTIFICATION AND STATISTICAL ANALYSIS

Unless stated otherwise in the STAR Methods section, the graphical representation and statistical analysis of the data were performed using GraphPad Prism 8 software (RRID:SCR 002798, www.graphpad.com). Details of the statistical analyses are provided in the figure legends and in Table S6. With the exception of (Figure 6A, 6C and S1A), all numerical data are presented as box and whiskers plots. The box extends from the 25th to the 75th percentile, the line represents the median, and the whiskers represent the minimum and maximum values. Dots represent individual specimens or biological replicates. In (Figure 6A), the relative proportion (in percent) of the most abundant bacterial genera in each biological replicate is presented as a stacked bar graph. In (Figure 6C), unweighted UniFrac distances of gut bacterial communities are presented as principal coordinate analysis (PCoA) plots. Ellipses show 95% confidence intervals. Each dot represents a biological replicate. In (Figure S1A), transcript levels are presented as superimposed bar graphs. The bar graphs represent the mean ± SEM and the dots represent the biological replicates. Blinding was not used in the course of our study. No data or subjects were excluded from our analyses, unless otherwise stated in the methods and figure legends.